2019

A Review of 2D and 3D Plasmonic Nanostructure Array Patterns: Fabrication, Light Management and Sensing Applications

Sujan Kassani

Katherine Curtin

Nianqiang Wu

Review article

Sujan Kasani, Kathrine Curtin and Nianqiang Wu*

A review of 2D and 3D plasmonic nanostructure array patterns: fabrication, light management and sensing applications

https://doi.org/10.1515/nanoph-2019-0158
Received June 1, 2019; revised August 29, 2019; accepted September 16, 2019

Abstract: This review article discusses progress in surface plasmon resonance (SPR) of two-dimensional (2D) and three-dimensional (3D) chip-based nanostructure array patterns. Recent advancements in fabrication techniques for nano-arrays have endowed researchers with tools to explore a material's plasmonic optical properties. In this review, fabrication techniques including electron-beam lithography, focused-ion lithography, dip-pen lithography, laser interference lithography, nanosphere lithography, nanoimprint lithography, and anodic aluminum oxide (AAO) template-based lithography are introduced and discussed. Nano-arrays have gained increased attention because of their optical property dependency (light-matter interactions) on size, shape, and periodicity. In particular, nano-array architectures can be tailored to produce and tune plasmonic modes such as localized surface plasmon resonance (LSPR), surface plasmon polariton (SPP), extraordinary transmission, surface lattice resonance (SLR), Fano resonance, plasmonic whispering-gallery modes (WGMs), and plasmonic gap mode. Thus, light management (absorption, scattering, transmission, and guided wave propagation), as well as electromagnetic (EM) field enhancement, can be controlled by rational design and fabrication of plasmonic nano-arrays. Because of their optical properties, these plasmonic modes can be utilized for designing plasmonic sensors and surface-enhanced Raman scattering (SERS) sensors.

Keywords: plasmon; nanostructures; nano-array; lithography; nanofabrication; sensor; surface-enhanced Raman scattering (SERS).

1 Introduction

Light interaction with metal nanostructures demonstrates unique properties that have drawn the attention of researchers, giving rise to an emergent field called plasmonics. Over the past two decades, advancements in both understanding physical phenomena and fabrication techniques have motivated and guided plasmonic nanostructure research and development. Because of recent advancements in fabrication and characterization techniques, plasmonic modes and their relationship to nano-architectures can be extensively studied. Understanding of the fundamental and optical properties is facilitating engineering of plasmonic nanostructures to meet technical needs and overcome challenges in medicine, biosensing, imaging, solar energy, catalysis, and optoelectronics.

Nanostructured materials have tunable physicochemical characteristics such as light absorption, color change, and electrical and thermal properties, whereas a bulk material is limited to its inherent material properties [1]. When light interacts with free electrons, the electron cloud is collectively excited as a plasmon [2]. Plasmon and light interaction allows for breaking the diffraction limit of light so it is localized in subwavelength dimensions. This localization of light in subwavelength dimensions produces enhanced optical near-field and strong electromagnetic (EM) field enhancement. If the localization of light takes place at the metal-dielectric interface as propagating waves, the excitation is known as surface

***Corresponding author: Nianqiang Wu,** Department of Mechanical and Aerospace Engineering, West Virginia University, Morgantown, WV 26506-6106, USA; C. Eugene Bennett Department of Chemistry, West Virginia University, Morgantown, WV 26506-6045, USA; and Department of Pharmaceutical Science, West Virginia University, Morgantown, WV 26506-9530, USA, Phone: +1-304-293-3326, e-mail: nick.wu@mail.wvu.edu. https://orcid.org/0000-0002-8888-2444
Sujan Kasani: Department of Mechanical and Aerospace Engineering, West Virginia University, Morgantown, WV 26506-6106, USA; and Lane Department of Computer Science and Electrical Engineering, West Virginia University, Morgantown, WV 26506, USA
Kathrine Curtin: Department of Mechanical and Aerospace Engineering, West Virginia University, Morgantown, WV 26506-6106, USA

plasmon polaritons (SPP), while if it takes place within the nanostructure, it is known as localized surface plasmon resonance (LSPR) [3]. Interestingly, these plasmonic phenomena have been applied for centuries without an understanding of the fundamental physical principles such as in dyes and optical windows.

A plasmon is typically excited on two types of substrates: (i) free-standing individual nanoparticles [4, 5] and their random aggregates [6], or (ii) chip-based two-dimensional (2D) or three-dimensional (3D) nano-array patterns. Colloidal particles and 2D and 3D nano-arrays differ in terms of their local EM field enhancement factors, fabrication, and use in real-world applications. Local EM field enhancement factors can reach 10^4–10^6 with metal nanospheres [7] while for colloidal aggregates, the EM field enhancement factors can reach high as 10^{14} [6, 8]. For colloidal nanoparticles, the plasmonic properties are tunable based on the dielectric environment, size, and morphology. Because of their large enhancement factors, colloidal nanoparticles have been extensively used in a variety of plasmonic-enhanced applications including solar energy conversion, photocatalysis, nanomedicine, and surface-enhanced Raman scattering (SERS) sensors.

Unlike colloidal nanoparticles, a 2D or 3D nano-array pattern is an ordered, periodic nanostructure geometry over a solid-state chip or substrate [9]. In 2D nano-arrays, the nano-array pattern is fabricated on a planar substrate. The coupling properties of the 2D nanostructure are analyzed by varying the distance between nanostructures. Therefore, in 2D arrays, coupling is restricted only in the horizontal direction and with a similar nanostructure which surrounds it, which permits coupling of same plasmon mode. Whereas in 3D nano-arrays, the pattern is fabricated on the top of another pattern or a film with a spacer layer in between. This allows 3D nano-arrays to exhibit additional plasmon resonance modes that are result of both horizontal and vertical coupling. Plasmonic coupling can also occur between the nano-array patterns in the top layer and bottom layer. 3D nanostructure coupling not only exhibits new plasmon modes, but also interesting optical phenomenon. Many nano-array patterns have been reported to generate tunable plasmonic properties such as: nanohole [10], nanorod [11], nanopyramid [12], nanoring [13], nanocube [14] and pyramid array coupled film [15]. In particular, the collective behavior of plasmons in nano-arrays produces a coherent optical response, which leads to strong and narrow spectral features [16]. The optical spectrum of a nano-array depends on size, shape, and periodicity of the structures, which provides great flexibility and tunability of plasmon and optical properties. The tailorable plasmonic properties in nano-arrays have opened ample opportunities for EM enhancement and light management with nano-arrays, making nano-arrays applicable in photovoltaic devices, photocatalysts, biosensors, nano-medicine, and optoelectronic devices.

Plasmonic nanostructures have been extensively used for two types of sensors [17]: surface plasmon sensors and SERS sensors. In surface plasmon sensors, the plasmon resonance is sensitive to changes in environmental refractive index induced by adsorption or binding of molecules on the material surface. Surface plasmon sensors result in a change in the plasmon resonance frequency, which can be used to generate calibration curves for sensing applications. SERS sensors operate by plasmonic amplification of Raman signals. Raman scattering is the result of inelastic light scattering and is used to detect vibrational and rotational properties of a molecule. The induced electric dipole moment for a Raman molecule is given by [18, 19]:

$$\mu = \alpha E \tag{1}$$

where α is the molecular polarizability and E is the electric field strength. The induced electric dipole moment of a molecule is directly proportional to the electric field strength of the medium where the molecule is present. Raman scattering intensity is directly proportional to the square of the induced dipole moment; therefore, when a Raman molecule is placed in a medium with a high electric field, the Raman signal is enhanced through a phenomenon called SERS [20]. When nanostructures are irradiated with light, the light can be confined in subwavelength dimensions and produce a large EM field for SERS enhancement. Because of the high enhancement factors, SERS is a very promising technique for sensing applications to overcome poor sensitivity and high background interference. Since SERS was first realized for single molecule detection in 1997 [21, 22], its application in the biosensing and nanomedicine fields has grown considerably. Over the past 20 years, the vast majority of SERS sensors have been engineered using colloidal nanoparticle SERS systems. Colloidal nanoparticles in SERS sensors systems are limited for use as in-solution detection probes, which can be subject to unwanted aggregation in biological matrices. Additionally, colloidal nanostructures, such as silver (Ag) and gold (Au) nanorods, have challenging synthesis methods that are difficult to reproduce. Compared to nanoparticles, nano-arrays are highly stable and ordered structures, and can extend the space for light management and EM enhancement. To further improve sensor performance and diversify material design, 2D and 3D nano-arrays have gained interest for SERS sensing substrates.

The increasing interest and application of plasmonic nano-arrays have motivated manufacturing nano-arrays with different architectures using traditional and emerging fabrication techniques. Electron-beam lithography, focused-ion lithography, dip-pen lithography, laser interference lithography, nanosphere lithography, nanoimprint lithography, and anodic aluminum oxide (AAO) template-based lithography have been used for nanofabrication. The availability of these lithography techniques endows researchers with powerful tools to create nano-arrays to support different plasmon modes that are excited and decayed in different manners, such as LSPR, SPP, Fano resonance, plasmonic whispering-gallery modes (WGMs), surface lattice resonance (SLR), and plasmonic gap mode. Each plasmonic mode has characteristic optical properties, unique distribution, and amplitude of an EM field. It is essential to understand the origin of plasmon excitation and decay, the optical responses of the plasmon, and the associated effects such as hot electron emission in order to fabricate and utilize plasmonic nano-arrays in a fashion of "device-by-design". Compared to colloids, nano-arrays exhibit unique advantages for sensing applications including long-range order and more advanced plasmonic optical modes for sensing.

This review article begins with introduction to lithography and fabrication techniques for 2D and 3D chip-based nano-array structures. Next, the origin and properties of plasmonic modes are discussed based on the nanoarchitecture. "Device-by-design" strategies using nano-arrays are examined for plasmonic and SERS sensor applications based on each plasmon mode. The goal of this review is to introduce the basic concepts and principles of each plasmon mode, and then demonstrate how plasmonic principles are used to design nano-array patterns and tune the optical responses, which provide a basis for light management and sensing applications.

2 Fabrication of nanostructure arrays

Conventional cleanroom-based photolithography (PL) is one of the most widely used and established fabrication techniques in the semiconductor and microfabrication industry. However, its spatial resolution is limited by the diffraction limit of light. The angle of diffraction depends on the wavelength of light used and the gap between the photomask and substrate. For these reasons, conventional photolithography is unable to produce high-quality nanoscale features, especially 2D and 3D hierarchical nanostructures. New nano-fabrication techniques have emerged to overcome the challenges associated with photolithography. These lithography techniques include electron-beam lithography, focused-ion lithography, dip-pen lithography, laser interference lithography, nanosphere lithography, nanoimprint lithography, AAO template-based lithography, and molecular stamping. An ideal nanofabrication technique is inexpensive, high throughput, high resolution, and provides great flexibility for tailoring nanostructure size and shape.

2.1 Electron-beam lithography (EBL)

EBL utilizes a modified scanning electron microscope (SEM) to write a custom nanoscale pattern by focusing an electron beam on an electron sensitive resist. EBL was first developed in 1967 [23] and has undergone technical development to achieve higher spatial resolution. Projection printing and direct writing are two schemes followed in EBL systems [24]. The primary difference between these methods is that the projection scheme uses a larger electron beam projected on to the mask, while in direct writing, an electron-beam spot is used to pattern the shape directly on the resist. There are two sub-categories of direct writing EBL systems based on the type of electron beam used. One is a Gaussian beam electron-beam system and the other is a shaped electron-beam system [25]. Gaussian electron-beam systems are commonly used because of their flexibility and fine spatial resolution [26]. This section will focus on the direct writing EBL system.

In a direct writing EBL system, a fine electron beam is focused on a wafer coated with an electron-beam resist. The electron-beam is focused using raster or vector scans and controlled with a blanker to turn the beam on and off. Once the pattern is transferred on to the resist, depending on the type of resist (positive or negative) the exposed part of the resist is etched using a developer. This leaves a nanostructure pattern that can be further processed with metal deposition and lift-off techniques. Because the electron-beam diameter is at the angstrom scale, the resolution of the EBL is very high for fabrication of 10-nm structures [27]. As the electron-beam is focused on a single point of pattern at a time, EBL requires a long processing time to transfer a full pattern onto the resist. This limits EBL throughput for large-scale production and large-area device fabrication even though EBL has high spatial resolution and is good for creating nanostructures with complex geometric shapes. Another drawback to EBL systems for commercial purposes is their high operating costs [28].

2.2 Focused ion beam (FIB) lithography

Similar to light, beams of electrons and ions can be used to alter the properties of resists for patterning. FIB are advantageous in nanostructure fabrication because of their high resolution [29]. Focused ion beam lithography uses a focused beam of ions to write the pattern instead of electrons, like in the case of EBL. FIB uses heavier ions such as He^+, Be^+ and Ga^+ for direct writing of the pattern, providing a stable and fine beam spot [30]. Whereas in EBL, electrons in the beam have larger Debroglie wavelengths and enlarged beam sizes due to scattering. In spite of these issues rectified in FIB, the heavier ions have less penetration depth, which reduces the high aspect ratio of the produced nanostructures [29]. FIB uses larger energies around 100 kV to 200 kV [31] to focus the ion beam and increases the energy deposition rate on the resist. This leads to higher exposure sensitivity [32]. Despite of the higher resolution, throughput and large area fabrication is still a challenge for the commercial production using FIB.

2.3 Dip-pen lithography (DPN)

DPN is a type of scanning probe lithography, where an atomic force microscope (AFM) tip is used to directly write a pattern by delivering chemical reagents directly on to the substrate. DPN was first introduced in 1999 as a tool for fabricating nanostructures [33]. Since then, it has been developed to pattern inks including organic molecules, colloidal particles, metal ions, and biological polymers [34]. A variety of substrate surfaces can be patterned using DPN, such as metals, insulators and semiconductors. DNP lithography is conducted in an inert environment making this technique an ideal candidate for pattering biological and soft organic structures. DPN offers high resolution as shown in the patterning of alkylthiols on gold substrate to achieve a 15-nm resolution with sharp tips [35]. Recently, parallel writing DPN has been developed, which addresses the complexity of engineering cantilever arrays by using a passive pen array [36]. One disadvantage of DPN is its throughput because it requires an inherent serial fabrication process and single pen configuration. Even though efforts have been made to use multi-pen configuration, DPN is an expensive, low throughput nano-fabrication technique, with a limited number of materials can be used in the ink for DPN.

2.4 Laser interference lithography (LIL)

LIL is similar to mask-less photolithography for fabricating nanostructures and is an effective method for large areas and high throughput fabrication [37, 38]. In conventional photolithography, monochromatic light is illuminated through a mask, and transfers a pattern on to the photoresist. In LIL, instead of using a mask to form a pattern, the pattern is formed from the superposition of multiple laser beams exposed onto a photoresist [39]. The interference pattern and electric field intensity is formed during the superposition of multiple laser beams. Because LIL does not use photomask, the patterns of different sizes and shapes can be easily modified by an interference principle. Also, the resolution of the feature size is not limited by diffraction of light that is commonly seen with mask techniques. The resolution is only limited by the wavelength of light being used during the pattern transfer [40]. However, not all shapes can be patterned using LIL, and the minimum period of nanostructures is limited to the half the wavelength of light. This requires the usage of deep ultraviolet (UV) light for smaller features [41], which makes LIL very expensive. For large exposure areas, the laser source should have a long coherence length and for higher resolution [42], lower wavelengths of light are needed. The light source specifications required for desired patterns makes the LIL challenging for large-scale fabrication.

2.5 Nanosphere lithography (NSL)

NSL is a flexible, inexpensive, high throughput technique for fabricating 2D and 3D nanostructures. In NSL, spherical colloids are transferred on to a substrate and dried to form a hexagonally closed pack (HCP) monolayer [43]. The monolayer is transferred on to substrate by various methods like dip coating [44, 45], spin coating [46, 47] and Langmuir-Blodgett [48]. This monolayer is used as a mask and the subsequent processing steps are performed to fabricate different nanostructure array patterns [13, 49]. Material is deposited through the interstitial spaces of the HCP beads and then the mask is removed by sonication leaving an ordered array of nanostructures on a substrate. The size and shape of the nanostructure can be easily changed by changing the bead size. NSL is a hybrid of a top-down and bottom-up approach, which offers a flexible fabrication [47, 50, 51]. Lithographic techniques like EBL, LIL and IBL are low throughput and have high sample costs making these techniques impractical for large-scale fabrication. Because of these challenges, many parallel lithographic techniques have been developed, with NSL among them. However, as an HCP monolayer is used as the mask for lithography, the shape and size of the angstrom scale nanostructure features are limited, so it is challenging to generate versatile nanostructure geometries and features.

2.6 Nanoimprint lithography (NIL)

NIL is a low-cost, high-resolution, and high-throughput technique for fabricating nanostructures. It was first developed by Chou in 1995 [52], and since then it has overcome many challenges to meet the practical industrial requirements. NIL demonstrated sub 10 nm imprinting in 1997 [53] and 2-nm structures fabrication [54], making it a promising technique for next generation lithography. It has been added to the International Technology Roadmap for Semiconductors (ITRS) for 32-nm and 22-nm nodes [55].

NIL uses molds to form nanostructures. In this technique, a stamp (or mold) with a specific pattern is mechanically pressed into the imprint fluid already coated on a substrate. The mechanical deformation causes the pattern to be transferred into the imprint fluid. After the hardening process, the stamp is removed and leaves the nanostructure pattern on the substrate. The resolution of NIL is limited by the mold pattern, and is not due to the diffraction limit of light such as in the case of photolithography. Therefore, the minimum feature size of the nanostructure pattern depends on the mold pattern feature size. Based on the type of imprint curing, there are two commonly followed nanoimprint processes: thermal NIL and ultraviolet (UV)-NIL [56]. Thermal NIL, the earliest form of NIL, utilizes a thermoplastic polymer as the imprint fluid. During the hardening step, the polymer is heated above the glass transition temperature to transfer the pattern. In the case of UV-NIL, a UV sensitive polymer is used as an imprint fluid. After the mechanical contact, the required dosage of UV light is illuminated on to the polymer to complete the hardening process. The applications of NIL are categorized into pattern transfer and polymer device applications. Its main applications are in optical storage devices, hard disk media devices, light emitting diodes, biosensors, microfluidic devices, and functional polymer devices.

2.7 Fabrication with AAO and other templates

The AAO template is a template assisted nano-patterning technique for low cost and high resolution [57] over a large area. The subsequent deposition of material through the template allows for the fabrication of nanostructures. The template is made by metal anodization in an acidic solution to form periodic metal oxide nanopores [58]. The thickness of the membrane and the periodicity of pores depend on the time of anodization and the voltage applied [59]. The flexibility of fabricating pore size which ranges from 7 nm to more than 300 nm make AAO a suitable template-assisted pattering for high-resolution fabrication [60]. This technique is applied to fabricate several nanostructures such as nanodots, nanorings, nanopillars, and nanotubes over a large area. Besides aluminum, titanium and zirconium metals can also be used to generate pore patterns by anodic etching. However, it is difficult to generate long-range-ordered periodic nano-array patterns in a large area. Furthermore, the geometry and layout of the nanostructure feature are limited by the fixed the AAO template because the template pores are round-shaped and laid out in a hexagonal pattern.

2.8 Outlook of development in nanofabrication techniques

Fabrication is a critical step for developing materials with tunable plasmonic properties. When designing nanostructures, the available fabrication techniques to produce and modulate the desired geometry and optical properties must be considered. A brief comparison of the fabrication techniques in terms of minimum feature size and throughput discussed are given in (Table 1). However, not one technique can meet all the needs for practical, large-scale production. An ideal fabrication technique should be low-cost, high-throughput, material and substrate independent, provide long-range order and have a sufficient minimum feature size. For example, techniques such as AAO templating and NSL produce high-throughput sub-100 nm features; however, long-range order remains a challenge. The drawbacks of each lithography technique inherently limit applications and the types of nanostructures that can be produced. These limitations need to be considered when designing plasmonic materials, as plasmon modes are highly dependent on the architecture. In the following sections, the origins of plasmon modes are discussed in terms of nanoarchitecture, design and fabrication.

3 Plasmonic modes and optical properties of nano-arrays

Similar to photons in a light wave, plasmons are quasiparticles composed of oscillating conduction electrons at the boundary between a metal and a dielectric and are generated by the electric field vector of incident light [68–71]. When the excitation light frequency matches the electron oscillations in materials with negative real and positive imaginary dielectric constant, SPR occurs. Understanding

Table 1: Summary and comparison of feature size and throughput by a fabrication technique [61].

Fabrication technique	Minimum feature size	Throughput	Reference
Photolithography (PL)	2–3 μm (contact and proximity)	Very high	[62]
	37 nm (projection printing)	High	[63]
Electron beam lithography (EBL)	Around 5 nm	Very low	[64]
Focused ion beam lithography (FIB)	20 nm with 5 nm lateral dimension	Very low	[63]
Dip pen lithography (DPN)	15 nm	Serial (low)	[35]
		Parallel (high)	
Laser interference lithography (LIL)	35 nm	High	[65]
Nanosphere lithography (NSL)	Sub 100 nm	Very High	[66]
Nanoimprint lithography (NIL)	2 nm	High	[54]
Anodic aluminum oxide (AAO) template	5 nm	High	[67]

and exploring the relationship between material properties such as size, shape, periodicity, and the dielectric with the optical response has resulted in a wide range of nanoarchitectures and applications including SERS [72, 73], sensors [74, 75], fluorescence enhancement [76], and refractive index measurements [77]. Because surface plasmon oscillations and their optical properties vary with the architecture and local environment, different types of surface plasmon oscillations, called plasmon modes, can arise. These plasmon modes are modulated based on the physical properties needed for the suited applications. Plasmon modes differ in fundamental properties such as near-field electric fields, mode volume, and bandwidth. SPR occurs in two fundamental modes, i.e. LSPR and SPP. Other plasmon modes, such as Fano resonance, plasmonic WGM, SLR, and the plasmonic gap mode, can be excited from the coupling and interaction of LSPR and SPP modes by controlling the nanoarchitecture.

3.1 LSPR

LSPR is a surface phenomenon generated by metal nanoparticles in which electrons oscillate collectively in resonance with incident light [5] (Figure 1A). The electric field around the localized plasmons is multiplied by several orders of magnitude, and intensity decays exponentially with distance. These resonances create a sharp optical absorption or scattering along with strong EM fields.

When metal nanoparticles are illuminated with light, the oscillating electric field induces coherent oscillations of conduction electrons and causes polarization of charge on the surface of nanoparticles [79, 80]. When the size of nanoparticles is small (<15 nm), resonance is dominated by absorption (Figure 1B) and when the size is larger (>15 nm) resonance is dominated by scattering (Figure 1C). The Mie solution based on Maxwell's equations explains the absorption and scattering cross-section by spherical particle whose diameter is less than wavelength of incident light [81].

$$\sigma_{\text{ext}} = 9\frac{\omega}{c}\varepsilon_{3/2}V_0\frac{\varepsilon_2(\omega)}{[\varepsilon_1(\omega)+2\varepsilon_m]^2+\varepsilon_2(\omega)^2} \tag{2}$$

where $x=2$ for sphere, $V_0=(4\pi/3)R^3$, ω is the angular frequency of the extinction radiation, ε_m is the dielectric function of the medium surrounding the metal nanoparticles, and ε_1 and ε_2 are the real and imaginary parts of the dielectric function of the metal nanoparticles, respectively.

The LSPR peak is highly dependent on the material, dielectric constant of surrounding medium, and size of nanostructure as given by Equation (2). The real part of the dielectric function determines the LSPR extinction peak position, while the imaginary part plays a role in the damping and resonance peak broadening. When $\varepsilon_1=-2\varepsilon_m$, polarization attain singularity and EM field is enhanced. Mie's theory is limited only to spherical particles. In 1912, Richard Gans generalized Mie's equation based on small particle approximation and found the absorption cross-section for prolate spheroid as [82]

$$\sigma_{\text{abs}} = \frac{\omega}{3c}\varepsilon_m^{3/2}V\frac{\left(\frac{1}{P_j^2}\right)\varepsilon_2}{\left\{\varepsilon_1+\left[\frac{1-P_j}{P_j}\right]\varepsilon_m\right\}^2+\varepsilon_2^2} \tag{3}$$

This gives extinction spectrum from both transverse plasmon mode and longitudinal plasmon mode. This equation shows the dependency of shape on LSPR peak wavelength, by incorporating shape dependent dielectric function $\frac{(1-P_j)}{P_j}$. For the shapes other than spheres and spheroids, the LSPR spectrum is studied numerically with finite difference time domain (FDTD) calculations. For noble metals such as Ag and Au nanoparticles, singularity condition ($\varepsilon_1=-2\varepsilon_m$) is met in visible region and

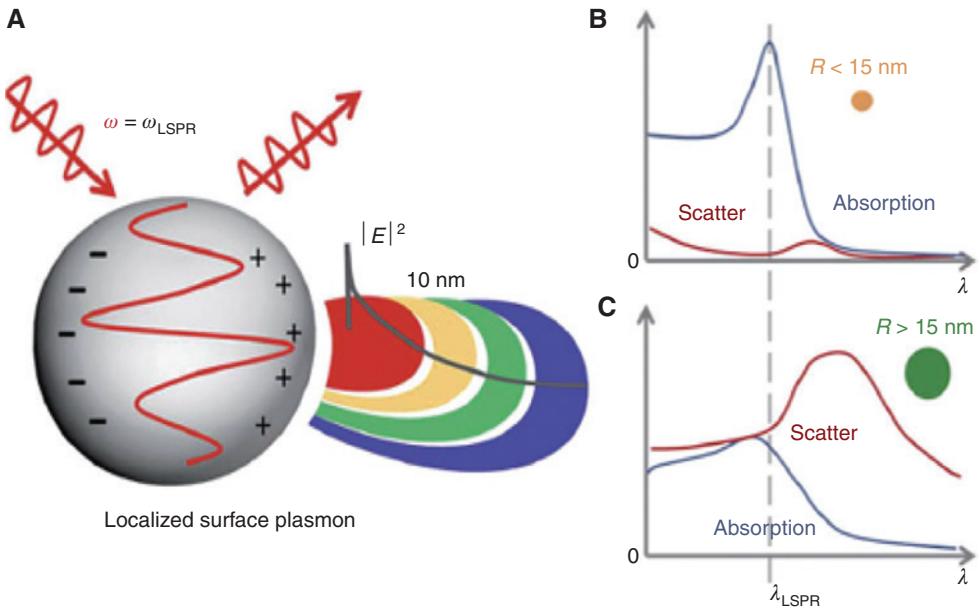

Figure 1: LSPR oscillation and optical properties.
(A) LSPR exists when the electron oscillations are in phase with the incident light frequency at the nanoscale (< wavelength of light). The collective oscillations result in enhancement of local EM field and sharp spectral response (scattering and absorption). (B) For nanoparticles smaller than 15 nm, spectral response is dominated by absorption. (C) For nanoparticles larger than 15 nm, spectral response is dominated by scattering (A, B and C reproduced from [78] with permission from The Royal Society of Chemistry).

near-infrared (NIR) where optoelectronic devices are operated and many biological applications are conducted. This gives noble metals an advantage over other materials for sensing devices. The sharp optical response and local EM field of LSPR phenomenon are used in many applications like biomolecule sensing, imaging, metamaterials, and resonance energy transfer.

The local EM field from the LSPR is directly proportional to the SERS enhancement. Thus, to improve the sensing performance, an SERS substrate is optimized with large density of localized plasmons known as plasmonic "hot spots" [83, 84]. Hot spots are areas of the plasmonic nanostructures where the local EM filed is enhanced enormously in comparison to its surroundings. Typically, hot spots are formed at the sharp tips and edges of nanostructures where there is a large charge density. As the distance between the metal nanostructures decreases, the EM enhancement at the hot spot increases exponentially [85]. When a Raman molecule is located in the hot spot, there is a tremendous enhancement in Raman signal as SERS. Typically, SERS enhancement is in the order of 10^4–10^8 colloidal nanoparticles, but nano-array substrates with high-density hot spots have enhancement ranging from 10^8 to10^{12} [86, 87]. This overall SERS enhancement from nano-arrays makes nano-arrays interesting for SERS sensing applications.

There are a variety of 2D and 3D nano-arrays that support plasmonic hot spots and LSPR modulation. Jung et al. [88] showed the fabrication of a well-ordered Ag nanodot array (Figure 2A) using an AAO template with uniform through-holes. The LSPR for an Ag nanodot array exists at the maximum extinction wavelength at around 500 nm (Figure 2B) and varies with the dot diameter. In this array, each dot acts as a hot spot. By using the AAO template, the diameter of the nanodots could be carefully controlled to tune LSPR. Nanotriangle [10] arrays were fabricated by NSL, which provided great control on periodicity and feature size. The fabrication of a nanotriangle is simple, where metal is deposited on to a monolayer of polystyrene (PS) beads. The SEM image and transmission spectra of a nanotriangle array is shown in (Figure 2C) and (Figure 2D), respectively. For nanotriangle arrays, the LSPR is due to the scattering of the light and exhibits a strong dip in the transmission spectrum. The hot spots in triangles reside at corners of the nanostructures. In another case, an Au nanodisc array [89] is fabricated by a combination of colloidal lithography and a nanoimprinting method as shown in (Figure 2E). A PDMS hemisphere stamp was fabricated and coated with a thin layer of Au to obtain the Au nanodisc array. The thickness of the Au disc was controlled by applied compression pressure during printing. By having control of the nanodisc thickness, the LSPR of the nanodisc could be tuned during fabrication (Figure 2F). The fabrication of nanopyramid [49] arrays is similar to the nanotriangle

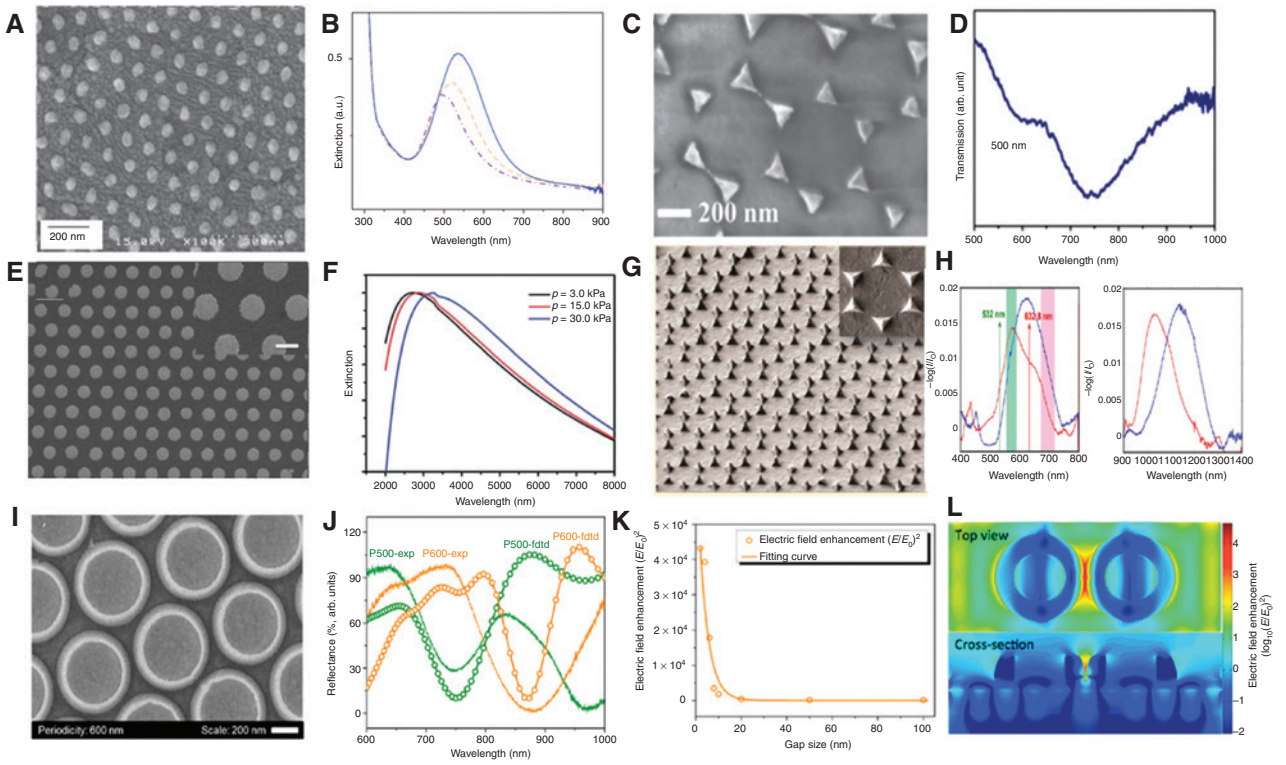

Figure 2: SEM images and optical properties of select nano arrays supporting LSPR.
(A) SEM image of Ag nanodot array on a glass substrate; (B) extinction spectra of Ag nanodot array on glass with different dot diameters (D = 42 nm (purple), D = 60 nm (orange) and D = 80 nm (blue), A and B reproduced from [88]); (C) SEM image of nanotriangle array; (D) transmission spectrum of triangles made from 500 nm polystyrene spheres (C and D reproduced from [10] with permission from the PCCP Owner Societies); (E) nanodisc array fabricated by combination of colloidal lithography and nano transfer printing (inset: magnified image); (F) extinction spectra of Au nanodisc array for different compression pressures (E and F reproduced from [89] with permission from The Royal Society of Chemistry); (G) SEM image (side view) of an Ag nanopyramid array (inset: top view); (H) Extinction spectra of Ag (red) and Au (blue) nanopyramid arrays (G and H reprinted with permission from [49]. Copyright (2013) American Chemical Society); (I) Au nanoring array (periodicity: 600 nm, outer radius: 500 nm, thickness: 50 nm, and height: 120 nm; (J) experimental (P500-exp) and FDTD-simulated (P500-FDTD) reflection spectra of Au nanoring arrays with periodicities of 500 nm and 600 nm, respectively; (K) gap-dependent EM field enhancement of a pair of Au rings; (L) EM field distribution of a pair of rings with a gap of 2 nm (I, J, K and L reprinted with permission from [13]. Copyright (2017) American Chemical Society).

array except for the thickness of the metal deposition. Thin metal deposition forms a triangle, while thick metal deposition forms a pyramid shape shown in (Figure 2G). The hotspots in pyramids reside along the edge and the corner of the structure, elucidating that there are two plasmon modes at different wavelengths as shown in Figure 2H. The longer wavelength plasmon mode is excited by the four corners and the shorter plasmon mode is due to the edge of the pyramid. Hot spots not only exist on the sharp areas of a structure they can also exist at the gaps between structures and are much more intense in confining EM fields. This is shown in an Au nanoring [13] array (Figure 2I). The EM field enhancement of an individual ring is around 5×10^2 whereas the EM field at the nanogap between two coupled nanorings has an EM field as high as 4.3×10^4 at a gap of 2 nm. NSL allows for the careful control of the optical reflection response and nanoring periodicity (Figure 2J). Using FDTD simulations, the nanogap between the nanorings exhibit varied EM field enhancements as shown in Figure 2K and L. Because of advanced nanofabrication techniques, these nanostructures can be fabricated and tuned in order to meet the desired optical properties. LSPR is the most commonly studied plasmonic mode for biosensor devices because LSPR generates strong near-field EM fields for SERS [90–92]. By utilizing plasmonic nanostructures, SERS enhancement factor can reach 10^{11}, which is sufficient for single molecule detection and highly sensitive SERS sensors [90, 93]. Conventionally used sensing techniques such as colorimetry and fluorescence are subject to high background interference, which reduces sensor sensitivity and performance. SERS can overcome interference from the sample matrix and water, as the Raman excitation wavelength and scattering wavelength can be

selected in the biological transparency window, where biological materials are not optically excited [94].

Over the past 20 years, SERS sensors have been extensively designed using colloidal nanoparticles coupled with Raman molecules as the signal transducer or "detection probe". In colloidal SERS sensing systems, recognition elements are bound to a nanoparticle probe either free in solution or over a substrate such as paper or plastic. SERS sensors using nanoparticles of various morphologies [90] have demonstrated good performance in clinical applications. To further improve performance and advance sensor material design, nano-arrays have emerged as SERS substrates. Compared to nanoparticles, nano-arrays provide long-range order, large surface area for sensing, and support a wider range of plasmon modes to enhance sensing performance [92]. For SERS sensors, the nano-array serves as a solid-state sensing substrate, where analyte recognition can occur on the material surface. When designing nano-array-based LSPR modes, it is critical to control the LSPR frequency via the fabrication technique. Additionally, morphology and nanostructure design should be chosen on the basis of maximizing the SERS enhancement factor. Because of the advancement in fabrication techniques, complex nano-arrays can be tuned to the desired optical properties. For sensors driven by LSPR modes, EM coupling between nano-array features is utilized to generate hot spots [91, 92]. In the nano-array sensors, nano-arrays can be used alone or coupled with colloidal nanostructures that serve as recognition elements. Systematic studies of LSPR and nanostructure morphology have been demonstrated in the importance of plasmonic modes and device design. For example, an Au nanotriangle array coupled with sandwich nanoparticles as reporter probes were investigated for SERS sensor performance. Three configurations of plasmonic nanostructures were investigated including: an Au nanosphere@MGITC@SiO_2 particles coupled on a planar Au film, an Au nanosphere@MGITC@SiO_2 particles coupled on an Au nanotriangle array, and an Au nanostar@MGITC@SiO_2 particles coupled on an Au triangle nano-array, where malachite green isothiocyanate (MGITC) is a Raman label. It was found that the greatest SERS enhancement factor of 10^6 was exhibited in the Au nanostar@MGITC@SiO_2 particles coupled on an Au triangle nano-array structure. The complexity of the structure results in strong confinement of the EM field into hot spots, which then can be coupled between local nanostructures. This design was applied for SERS detection of breast cancer biomarkers, vascular endothelial growth factor (VEGF), with a limit of detection (LOD) of 7 fg/ml [95].

Similar configuration designs have also been explored using coupling between Ag nanopyramid arrays and Au nanostars [96], nanohole arrays and Au nanostars [97] and Au nanotriangle array@graphene [98] and 3D dimensional Au nanoparticle-monolayer graphene-Ag hexagon nano-arrays [99]. Complex structures such as nanostars [100, 101], nanocubes [102], nanotriangles [103], and nanorods [101, 104] are advantageous over simple structures such as nanospheres because of concentrated EM fields at edges and tips of the structure [92]. In these structures, the coupled nanoparticle and nano-array are both optically tuned and optimized to generate hot spots for sensing.

3.2 SPP

SPPs are surface EM waves that propagate along the metal-dielectric interface as shown in (Figure 3A). These waves are visible or infrared waves whose EM field decays with distance into both mediums (Figure 3B) [106–108]. Unlike LSPR, SPP cannot be excited directly by incident light due to the high momentum requirement. The classic example of SPP is the Kretschmann configuration, where an Au film is coupled to a prism and demonstrates optical excitation of SPP on a metal surface [109, 110]. The large refractive index prism enables an evanescent field through attenuated total reflection to excites plasmons (Figure 3C). The prism makes the horizontal wave vector components of the incident light couple to the propagating SPP wave vector, as long as the two wave vectors match at a certain incident angle (Figure 3D).

From Maxwell equations, the SPP dispersion relation can be expressed as [111, 112]

$$K_{\text{spp}} = k\sqrt{\frac{\varepsilon_d \varepsilon_m}{\varepsilon_d + \varepsilon_m}} \tag{4}$$

The nonlinear characteristic nature of SPP results in a momentum mismatch between light and SPP. This mismatch can be overcome by coupling light and SPP modes at the condition

$$\varepsilon_d + \varepsilon_m = 0 \tag{5}$$

At this condition, the real part of the dielectric constant is negative and denominator in the above equation is zero resulting in a resonance condition with resonance frequency $\frac{\omega_p}{\sqrt{1+\varepsilon_d}}$, where ω_p is the bulk plasma frequency. This resonance generates a surface plasmon propagating wave along the metal-dielectric interface and decays

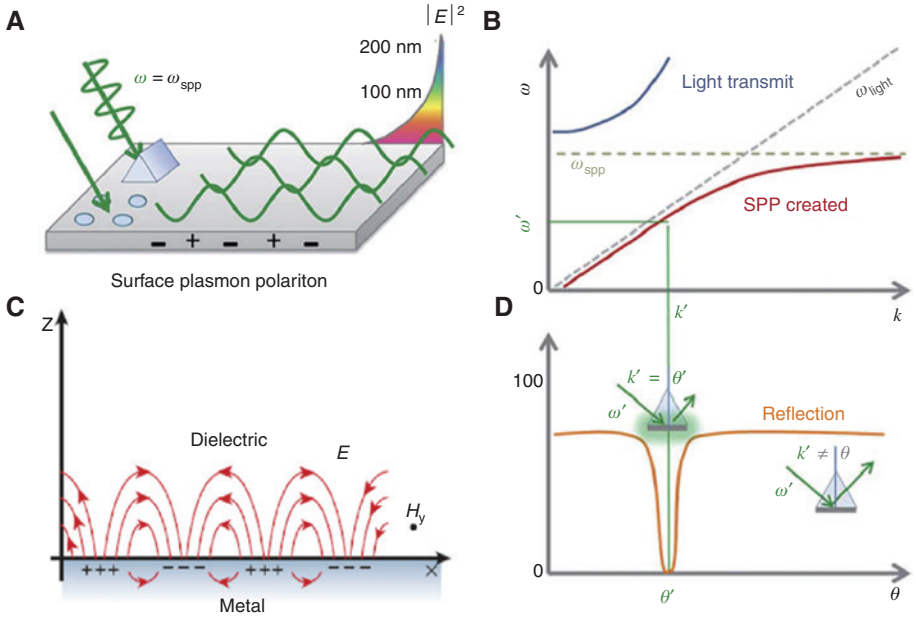

Figure 3: Electron oscillation and excitation conditions of SPP.
(A) SPP wave is propagating charge wave, generated along the metal dielectric interface which couples with an EM field. The amplitude of SPP wave exponentially decreases away from the interface. The SPP can only be excited (B) at certain wave vectors and exists as a field that decays evanescently from the surface. The momentum matching condition leads to the SPP resonance (D) only existing at certain incident angles (A, B and D reproduced from [78] with permission from The Royal Society of Chemistry). (C) Illustration of SPP wave, comparing relative penetration depth of SPP into metal and dielectric medium (reproduced from [105]).

exponentially with distance. The penetration depth of an EM field in a dielectric is longer than the depth in metal and this difference is more prominent at longer wavelengths [113].

The distinct behavior of SPP, which allows the control of light at the nanometer scale, which has opened potential applications in photonics [114, 115], SERS [20, 116, 117], spectroscopy [118], data storage [119] and sensors [120, 121]. Extraordinary optical transmission (EOT) is a phenomenon where transmission of light is greatly enhanced through an opaque metallic film due to the excitation of SPP in a nanohole array pattern on the film [114]. Laser interference lithography was used to fabricate an Au nanohole array [122] as shown in Figure 4A. The transmission peak is very sensitive to the hole periodicity and dielectric medium. When molecules are adsorbed on the substrate with a nanohole array, the transmission peak shifts due to change in the dielectric properties of the surface from newly adsorbed molecules [123] as shown in (Figure 4B).

Spectrum filtering is one of the applications of SPP. Liang et al. [124] has demonstrated an ultra-thin bandpass filter with high angular tolerance and transmission efficiency. The periodic metal-dielectric-metal geometrical design (Au-Si_3N_4-Au) was fabricated by FIB as shown in Figure 4C, and exhibits narrow optical transmission. The incident light is coupled to the plasmon mode through the slits on the top layer. The bottom Au grating converts the confined plasmon to propagating waves and transmits the incident light to far field. The transmission wavelength can be tuned by changing the geometrical parameters of the slit for filter applications (Figure 4D). Likewise, an Au film evaporated onto NSL silica spheres forms a periodic corrugation to the Au layer (Figure 4E). This corrugation acts as a grating which couples the far field to SPP modes [125]. In this work, the SPP-assisted visible light emission is detected and SPP extraction efficiency is evaluated by studying the polarization properties (Figure 4F).

SPP modes have been employed in sensing applications for label-free biomolecule detection. SPP differs from LSPR for sensing because SPP propagates hundreds of micrometers along surface. This gives a unique advantage where the incident laser can avoid direct exposure on the measured sample. This reduces interference from strong background noise and damage from the high energy laser on the sample [127]. For example, a plasmonic narrow groove gratings have been used in a miniaturized SPR sensor (Figure 4G) [126]. The incident light is coupled into surface plasmons without the use of prism-coupling (Kretschmann configuration). The further rigorous coupled wave analysis simulation was done to determine the wavelength at which the plasmon resonance occurs with changes in the groove parameters (Figure 4H). The

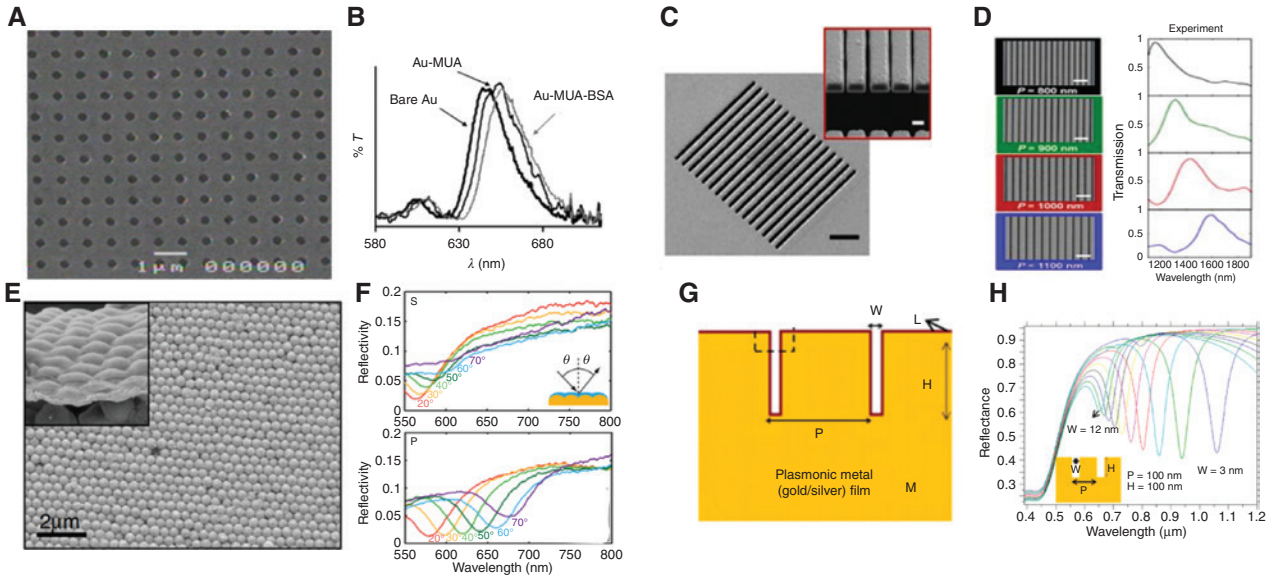

Figure 4: SEM images and optical properties of nano arrays supporting SPP.
(A) SEM image of gold nanohole array fabricated by LIL (reproduced from [122]); (B) transmission spectra and the effects of molecular adsorption on EOT (reprinted with permission from [123]. Copyright (2004) American Chemical Society); (C) plasmonic bandpass filter by MDM stack array. Inset: cross-section view; (D) measured transmission spectra for various periodicity (P), (800 to 1100 nm) and slit width (L) (C and D reproduced from [124]); (E) SEM image of thick gold film on silica spheres, inset: image after silica spacer deposition; (F) polarized reflectivity spectra of plasmonic sample at different incidence angles (20°–70°), top figure: s-polarized. Bottom figure: p-polarized (E and F reproduced from [125]); (G) schematic showing narrow groove plasmonic nanograting structure with groove width "w" and periodicity "p"; (H) effect of nanograting dimensions "w" on the plasmon resonance dips in the reflectance spectra for narrow groove Au nanogratings (G and H reprinted with permission from [126], © 2011 Optical Society of America).

narrow groove nano-could potentially lead to the development of more robust SPR sensors as it does not require angular dependence. In a study by Kalachyova et al. [117], an SERS substrate composed of a sinusoidal Ag grating is used to excite SPP modes. Experimental and theoretical results demonstrate an SERS enhancement factor up to 10^5 was achieved by tuning the structural parameters. Although this work did not demonstrate SERS sensing, the enhancement factor is sufficient for SERS sensing applications [117]. A similar structure, a 1D Ag/SiO_2 sinusoidal nanograting, has been applied for SERS detection of trace TNT. EM field enhancement was calculated as 10^5, while experimental evaluation demonstrated a 10^4 enhancement and TNT detection with an LOD at 10^{-5} M [128].

SPP and LSPR coupled sensor designs are based on the understanding on plasmonic coupling to create local hot spots, enhancing the near-field intensity in the nanostructure to improve SERS LOD and sensor performance [129, 130]. For example, LSPR and SPP modes were coupled in an Au nanodisc array patterned by EBL on an SiO_2 spacer and Au film. SERS enhancement factor experiments demonstrated the factors were 7.2×10^7 for Au and 8.4×10^8 for Ag [129]. SPP and LSPR coupling has been also demonstrated in other structures such as 2D metal-coated dielectric gratings with SERS enhancement of 2×10^9 [130]. In this study, a combination of experimental work and FDTD simulation demonstrated how morphology affects plasmon coupling, hot-spot regions, and SERS enhancement factor FDTD simulation among other calculations. This serves as a very useful tool when designing, optimizing, and characterizing nano-array architectures, especially with SPP and LSPR modes. When designing nanostructures for SPP and LSPR coupling, the two modes must be carefully controlled by morphology, periodicity, local refractive index, and angle in incident illumination. The resulting coupling causes a repulsion in the resonances and enhancement of the near-field and is evident in the extinction cross section by two primary resonances [131].

3.3 Fano resonance

Fano resonance is the interaction between a narrow discreet state (Figure 5A) and a broad continuum (Figure 5B), producing a narrow asymmetric spectral shape with resonant suppression and enhancement [133–135]. Constructive interference of the two modes results in enhancement of the resonance, while destructive interference results in the suppression of the resonance. The resulting optical

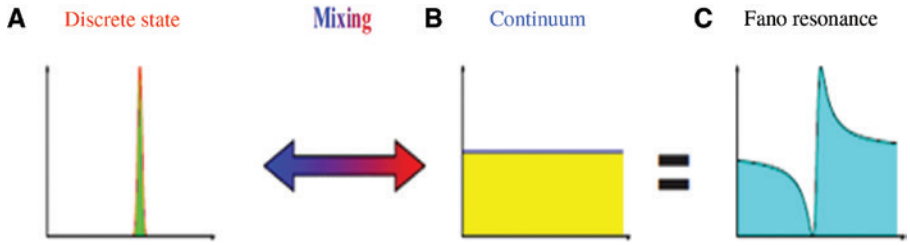

Figure 5: Illustration of Fano resonance.
(A) Lorentzian line shape of discrete level; (B) flat continuous background; (C) superposition result of two levels (discrete and continuum) to form a Fano resonance line shape (A, B and C reprinted with permission from [132]. Copyright (2010) by the American Physical Society).

spectrum is given by the Lorentzian formula, which describes the superposition of the two modes. The absorption spectrum shape of Fano resonance is given by [136]:

$$\sigma(E) = (t_D)^2 \frac{(q+\xi)^2}{(1+\xi^2)} \tag{6}$$

where E is the energy, t_D is the non-resonant transfer amplitude, q is the shape parameter that determines the asymmetry of the profile, $\xi = \frac{2(E-E_0)}{f}$ where E_0 and f are the energy and resonance width, respectively.

A Fano resonance can be derived from the Mie theory for a single spherical plasmonic particle. The magnetic and electric amplitudes depend on size parameter. Considering a small size $q<<1$ and non-magnetic particle ($\mu = 1$), Rayleigh scattering yields [137]:

$$Q_{sca} = \frac{8}{3}\frac{|\varepsilon-1|^2}{|\varepsilon+2|}q^4 \tag{7}$$

With increase in size ($q>1$), eigen modes increases creating extra resonances. When $\varepsilon>1$, all the resonances are broad and there is no possibility of Fano resonance. When $\varepsilon<0$ the resonance is broad at the same time for $\varepsilon<0$ and $q>1$, the resonance is weakly damped for dissipative materials (noble metals) and have a narrow resonance. These two resonances coexist over a window of "ε", forming Fano resonance.

The Fano resonance phenomenon exists in plasmonic nanostructures [138–140] where the continuum plasmon resonance couples with a discrete state to form a Fano resonant mode (Figure 5C). The discrete state can be the excitation of a molecule [141], excitation of a dark plasmon mode [142], or excitation of a diffraction channel [143]. Fano-like resonance is present in a nanoring cavity array (Figure 6A), where there is coupling between LSPR of the nanostructure and the Bloch wave-SPP of the periodic array. The coupling results in a sharp Fano resonance centered at 698 nm (Figure 6B) [144]. In a hexamer structure (Figure 6C), there exists only dipolar plasmon resonance (Figure 6D), but when a central Au nanoparticle is brought into close proximity of the six nanoparticles, the hybridization of central particle dipolar plasmon with hexamer dipole resonance generates Fano resonance [147]. The Fano resonance is formed from the destructive interference between the broad supper-radiant mode and the narrow sub-radiant mode. The high Q factor of the Fano resonance in a binary silicon nanohole array (Figure 6E) has been used in high-performance optical modulators [145]. In a binary nanohole structure, each hole array has a lattice collective resonance mode with different resonant energies, and they hybridize to generate a bright mode and a dark mode [148]. The interaction of the bright and dark mode forms the sharp asymmetric Fano resonance as shown in (Figure 6F). Unusual Fano resonance is found in plasmonic nanograter fabricated by the direct writing FIB technique (Figure 6G and H) [146].

Fano resonance has been applied in the fields of biological sensing, lasing, medicine, metamaterials, and optoelectronic devices. This is because of the unique nature of Fano resonance to efficiently confine light and it having a narrow optical feature [149]. Sensors utilizing Fano resonance are based on the weak coupling and interference between sub-radiant and radiant LSPR modes or SPP modes, and use peak shift for sensing recognition [150]. Fano resonance is typically used to enhance the sensitivity of conventional LSPR and SPP sensors by amplifying the EM fields [150, 151]. Unlike SPP and LSPR modes, Fano resonance exhibits very narrow, asymmetric resonant peaks with large EM field enhancement [151]. This feature of Fano resonance is sensitive to changes in the local environment so that the Fano resonant materials can be applied as optical sensing substrates [151].

In terms of design, Fano resonance originates from symmetry breaking in nanostructures, which promotes interference between the sub-radiant and radiant modes. This understanding guides nanostructure designs for Fano resonance. For nano-arrays, the metallic elements generate broad radiant plasmonic modes while sub-radiant

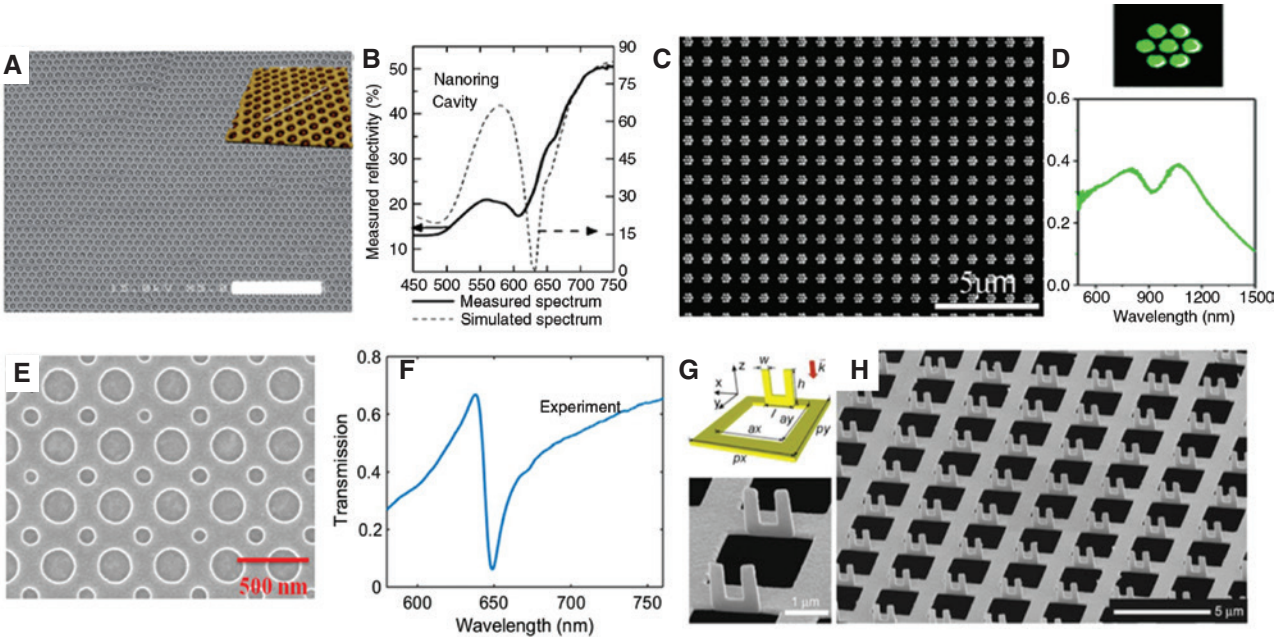

Figure 6: SEM images and optical properties of nano arrays supporting Fano resonance.
(A) SEM image and (inset) AFM topography of a nanoring cavity array; (B) comparison of simulated and measured reflection spectra of nanoring cavity (A and B reproduced from [144] with permission from The Royal Society of Chemistry); (C) SEM image of gold heptamer sample fabricated by electron-beam lithography; (D) a normal view of the heptamer structure (top), extinction spectra (bottom) of a gold heptamer with interparticle gap <60 nm (C and D reprinted with permission from 142]. Copyright (2010) American Chemical Society); (E) SEM image of binary silicon nanohole array; (F) measured transmission with bigger hole radius = 50 nm and smaller hold radius = 110 nm of a binary silicon nanohole array (E and F reproduced from [145]); (G) schematic (top), high magnification SEM image (bottom) of (H) SEM image (large area) of Fano resonances from vertical U-shaped SRRs standing along horizontal rectangular hole arrays in a free-standing metallic film (G and H reproduced from [146]).

modes exist by near-field coupling of the nanostructures. Both of these elements can be tuned by geometric and structural variation. Fano resonance sensors for LSPR mode enhancement have been designed with Ag nanocubes [152], nanorings coupled with nanodisks [153], and nanoclusters [154]. Figure 7A shows the plasmonic sensor structure based on a metal-dielectric-metal waveguide. The upper cavity couples weakly and the lower cavity couples strongly with the input wave, exciting subradiant and superradiant modes, respectively [149]. Thus, Fano resonance is achieved by coupling between these modes. The resulting transmission peak is sensitive to the local refractive index, allowing for refractive index-based sensing applications (Figure 7B). Due to the narrow resonance window, sensors based on refractive index changes are highly sensitive. Figure 7C shows the experimental demonstration of detecting biomolecule with the naked eye and Fano resonance [142]. The plasmonic chips with Fano resonance are functionalized with a biomolecule and a notch filter is tuned to filter light outside the resonant transmission peak. The blue curve shows the transmission spectra of the functionalized chip. When the monolayer of mouse immunoglobulin (Ig)G antibody is captured, there is a 22 nm shift in the plasmonic resonance, allowing the overlap with a notch filter. This results in the drastic reduction of transmission (Figure 7D), which can be noticed with the naked eye. Although Fano resonance has not been demonstrated in SERS sensors, Fano resonance enhancement of SPP and LSPR modes is of interest for SERS. As the peak shift typically associated with Fano resonance sensors and refractive index change is very small, the EM field enhancement via Fano resonance could still be utilized for SERS without great changes to the plasmon peak. Fano resonance using a nanograter structure was also applied for refractive index sensing. The Fano resonance exhibited in this structure demonstrated sensitivity at 2040 nm per RIU and Fano resonance extending into the NIR region [146].

3.4 Plasmonic WGM

WGM resonances occur when an EM field becomes trapped at the surface of a structure due to total internal reflection [156–159]. They are gallery modes specific to a cavity and highly dependent on the geometry of the cavity [160, 161].

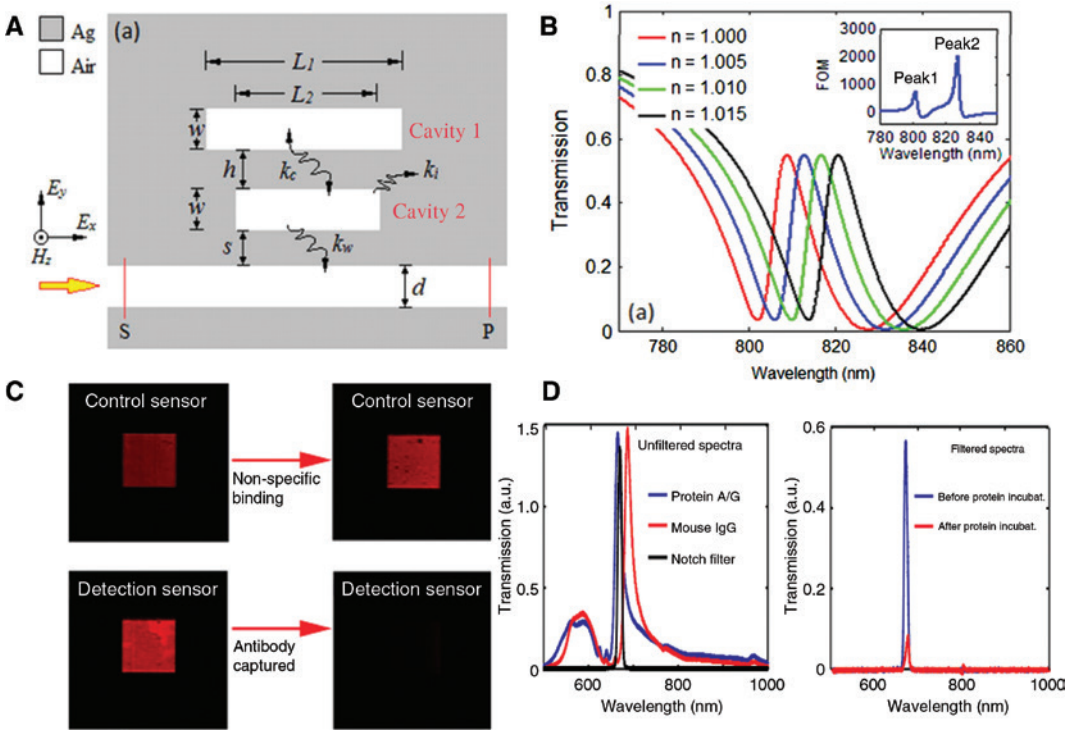

Figure 7: Select MIM nano arrays supporting Fano resonance for sensing applications.
(A) Schematic layout of a metal-dielectric-metal based plasmonic resonator; (B) the sensing response of Fano resonance peak shift with change in refractive index, inset: corresponding FOM variation (A and B reproduced from [149]); (C) comparison of CCD images with transmitted light obtained from detection and control sensors. Transmitted light intensities drop with capturing antibody; (D) (left) transmission spectra of before (blue curve) and after (red curve) capturing of the antibody. Spectral characteristic of the notch filter (green curve) is shown. (right) Transmitted light intensities in the presence of the notch filter is given before (blue curve) and after (red curve) the capturing of the antibody (C and D reproduced from [155]).

WGM resonators have a high-quality factor (Q), making them a potential candidate for biosensors. When the length of the optical path matches the integer number of the wavelength, a standing wave is formed inside the cavity. At this resonance condition, the mode is confined in the dielectric medium, and a small portion extends outside, which is very sensitive to the surrounding environment. The change in the resonant frequency with molecule is sensitive and used as WGM sensors. The performance of a WGM resonator is measured by a quality factor *(Q)*, defined as:

$$Q = \frac{\omega_0}{\Delta\omega_{\mathrm{FWHM}}} \tag{8}$$

where ω_0 is the angular resonance frequency and $\Delta\omega_{\mathrm{FWHM}}$ is linewidth of the frequency (full width at half maximum). However, for single molecule detection the resonance shift is not sensitive enough. The resonance shift is given by [162]:

$$\frac{\Delta\lambda}{\lambda_r} = \frac{\alpha |E(r)|^2}{2\int \varepsilon_r |E(r)|^2 \, \mathbf{dV}} \tag{9}$$

where r represents molecular binding site, E is the WGM electric field strength, α is the polarizability of the molecule, λ_r is the laser wavelength, ε is the permittivity of the cavity. From Equation (9), the wavelength shift is proportional to the electric field strength $|E(r)|^2$. Plasmonic nanostructures with high electric field strength are thus used in WGM resonators to excite a hybrid plasmonic WGM mode, which has higher sensitivity compared with a normal WGM resonator.

WGM resonators can be made in various shapes, including spheres [163–165], rings [166], disks [167, 168], and toroids [169] and they can be composed of various materials, including polymers, metal oxides and silicon [161]. To improve sensitivity, a hybrid plasmonic WGM is designed by incorporating plasmonic nanostructure in a WGM resonator. Plasmonic WGM is a hybridized mode between surface plasmons and WGMs, which exhibits the combined benefits of plasmonic localization with high Q-factor microcavities. However, the incorporation of plasmonic structures in a random way may not support the WGM mode itself. Hence, periodic arrays of plasmonic nanostructures were coupled, which allows a constructive

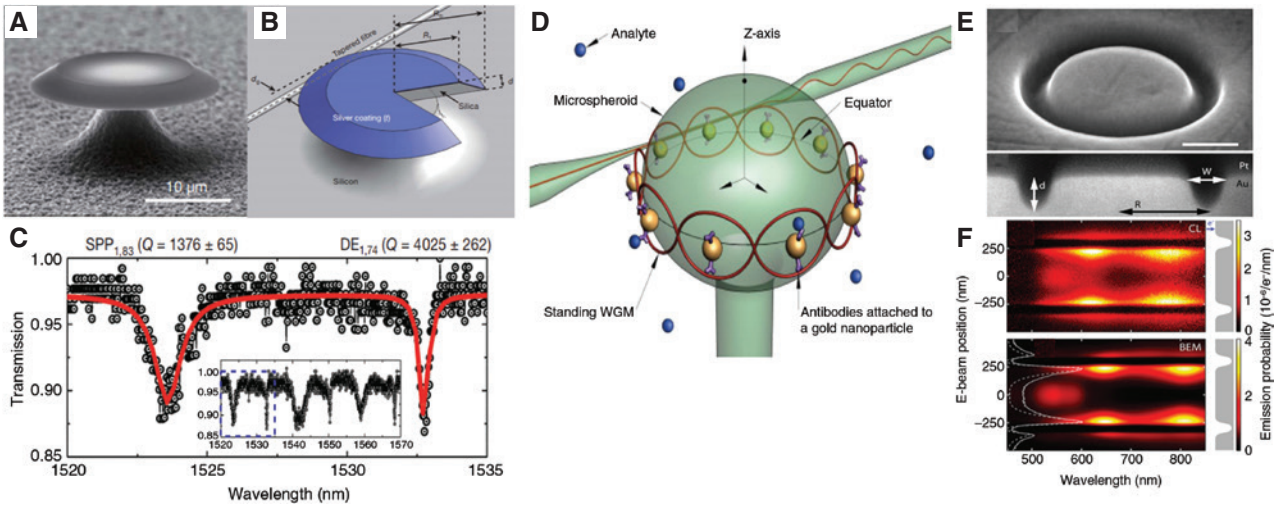

Figure 8: WGM resonator configurations and associated optical properties.
(A) SEM image of an Ag-coated SPP whispering-gallery microdisk resonator; (B) Schematic of SPP microdisk resonator with a tapered optical fiber passing under its edge; (C) *Q*-factor measurements for Ag-coated microdisk resonators. Normalized transmission spectrum showing the highest measured SPP *Q* factor of 1376 ± 65 and a dielectric resonance with a *Q* factor of 4025 ± 262 (A, B and C reproduced from [170]); (D) illustration of an oblate spheroidal WGM resonator with functionalized periodic nano-plasmonic epitopes, that is driven at a frequency that produces a symmetric standing wave (reprinted with permission from [171] © 2012 Optical Society of America); (E) SEM image of FIB-fabricated ring groove in single-crystal Au. Top view (top image), side view (bottom image); (F) spatial mapping of modes by cathodoluminescence plasmon microscopy (reprinted with permission from [172]. Copyright (2009) American Chemical Society).

interference, improving the sensitivity of sensor. Figure 8A shows a plasmonic microdisk cavity structure composed of a core silica disk microcavity covered with a thin layer of Ag (cladding), which has demonstrated a *Q* value as high as 1376 [170]. Initially disk-shaped photoresist pads were fabricated by photolithography, and etched in buffer oxided etch (BOE). Acetone is used to remove the photoresist, and the remaining silicon disk is suspended by an undercut formed during the isotropic etch. Figure 8D shows that the periodic plasmonic epitopes are attached to the surface of WGM microcavity to improve the performance of the sensor [171]. The addition of regular plasmonic epitopes on the diameter of the WGM resonator form a hybrid mode which boosts the frequency shift enhancement. Figure 8E shows a ring-shaped nano-resonators fabricated by FIB patterned in a single-crystalline Au, which is used to analyze the resolution of the WGM of a plasmon ring cavity [172]. Scanning cathode luminescence spectroscopy and EM modeling has been used to obtain the spatial and spectroscopic information (Figure 8F).

WGM sensors typically operate by realizing changes in the resonant frequency or linewidth. These changes arise from changes in the local refractive index induced by the analyte of interest. This form of sensing requires the device to be highly sensitive to changes in the refractive index [161, 163]. Examples of sensors operating in this manner include viral [164] or protein detection [173], refractive index sensing [166], and environmental monitoring [168]. Even though WGM sensors have high sensitivity, it is challenging in achieving high signal-to-noise ratio due to the presence of noise in the optical measurement [174]. The performance of the WGM resonators can be improved by incorporating plasmonic nanostructures, where both the *Q* factor of the WGM and the EM field of the plasmonic structure are completely utilized for applications. In this way, extremely low photon loss rate is achieved in plasmonic structures, opening new research in the areas of nonlinear optics and quantum optics [175, 176]. Because of the high enhancements from WGMs, plasmonic WGM sensors have the potential for single-molecule and label free detection [161, 163].

Sensing by changes in resonant frequency and linewidth is difficult as calibration and data analysis are more complex [161]. However, when WGM resonators are coupled with plasmonic nanostructures, the plasmon can enhance the local EM field remarkably. Because of this, WGMs paired with nanostructures can be applied in high-sensitivity SERS sensors. In a computational work, the SERS enhancement factor is calculated for a microsphere plasmonic WGM structure. Because Raman scattering radiation overlaps with WGM resonance, microspheres have made an SERS enhancement factor as high as 10^8 [165]. In order for the WGMs to be enhanced by the plasmon, an EM field should be tangent to the resonator surface.

3.5 SLR

SLR arises from optical coupling of LSPR modes in arrays of metallic nanoparticles (Figure 9A) [178, 179]. Compared the optical absorption of LSPR (Figure 9B) from single nanoparticles, SLR from nanoparticle arrays has much narrower optical spectrum features (Figure 9C), making this mode desirable for light absorption applications and sensing [180]. Like LSPR, the SLR modes can be tuned along the UV-Vis and NIR spectrum by variation in morphology, particle size, material, refractive environment, and periodicity [178, 179].

The coupled dipole approximation (CDA) is instrumental in understanding the difference in extinction cross-section between LSPR and SLR. In this approximation for SLR, the dipole sum provides an additional degree of freedom (dependent on periodicity, particle size, etc.) to govern the width of the SLR mode [178]. The effective polarizability (α_{eff}) and the extinction cross section (C_{ext}) are given by:

$$\alpha_{\text{eff}} = \frac{1}{\frac{1}{\alpha_s} - S} \tag{10}$$

$$C_{\text{ext}} = 4\pi NkIm(\alpha_{\text{eff}}) \tag{11}$$

where α_s is the isolated nanoparticles polarizability, S is the retarded dipole summation from other particles, N is the number of particles, and k is the wavenumber of incident light.

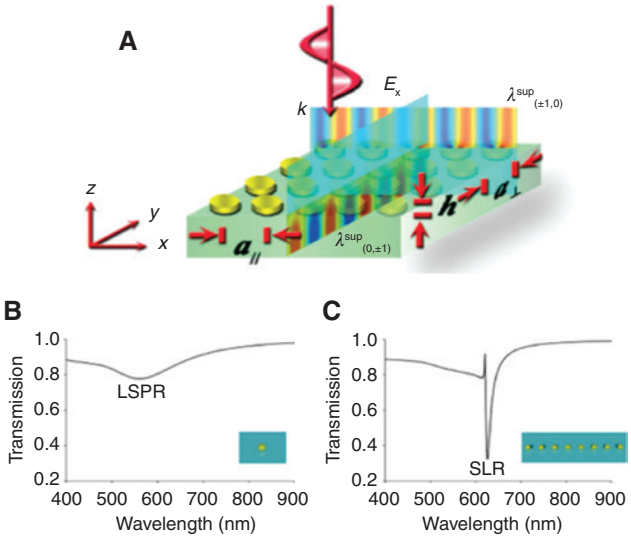

Figure 9: Electric field distribution and optical transmission of SLR. (A) Orthogonal and parallel coupling in SLR (A reproduced from [177] with permission from The Royal Society of Chemistry). Comparison of LSPR and SLR in calculated transmission spectra schematic of structures considered: (B) single particle; (C) a periodic 1D chain (reproduced from [178], https://pubs.acs.org/doi/abs/10.1021/acs.chemrev.8b00243 further permissions related to the material excerpted should be directed to the ACS).

Nano-arrays are designed with assistance from CDA to support SLR. The primary control parameters to realize SLRs are the particle size and the lattice constant as they control the coherent interaction of the plasmons [178, 179, 181]. An increasing lattice constant results in a more negative dipole sum, which redshifts the resonant frequency and decreases FWHM, while decreasing diameter will blue shift the resonant frequency. SLR supports both orthogonal and parallel EM coupling, which is dependent on the relationship between incident light propagation and diffraction wave propagation [179, 181]. Orthogonal or parallel coupling occurs when the light polarization is either vertical or parallel to the diffraction wave [181]. These characteristics allow for SLR modes to be easily tuned to desired wavelengths along the EM spectrum.

Many nano-array structures and materials have been investigated for SLR modes. Symmetric and asymmetric nanodisc dimers [182], nanoparticle arrays, and square, hexagonal, and honeycomb [180] configured nanoparticle arrays have been shown to support SLR. Lattice constant, morphology, and size are primarily studied to elucidate the origin and magnitude of SLR. Interestingly, spatial arrangement of arrays has no effect on SLP magnitude and position. Nanoparticles arranged in square, hexagonal, and honeycombs configurations exhibited similar SLR wavelength and diffraction edge, which demonstrates periodicity and lattice constant is a factor driving EM coupling [180].

Because of the strong narrow plasmon resonance, SLR is an appealing mode for optical sensing, photovoltaics, and photocatalysis. For light harvesting applications, the SLR of nanoparticle arrays enhances photoelectron emission in solar cells. The nano-array structure can achieve comparable photocurrent density to densely packed nano-arrays, therefore a much lower density of nanoparticles is needed. Additionally, photoelectron emission can be controlled by tuning the size, shape, and periodicity of the nanoparticle array [183]. Coupling metallic nano-arrays with semiconductor materials is promising for improving the optical absorption efficiency [184] and excitation of electrons [185] for photocatalysis.

For sensing, the sharp spectral feature of SLR can improve LOD and figure of merit (FOM) for optical sensors compared to using LSPR modes for plasmonic sensors. Single nanoparticles for sensors are limited by the high FWHM of the plasmon resonance. Broad plasmon modes are subject to lower sensor performance because it is more difficult to resolve small changes in plasmon frequency [179]. SLR modes of nanodisks [186, 187] and

nanoparticle [188] arrays have been developed for potential sensing applications. Sensors operating with SLR modes typically utilize shifts in the plasmon position for chemical or biological recognition [178]. For SLR sensor application, there are practical design considerations that must be optimized and considered. Refractive index mismatch between substrate and the surrounding environment, such as buffer, can adversely affect the EM field symmetry, and cause the increased linewidths [178, 179]. To overcome such challenges, architectures have been designed to include additional contributions from Fabry-Perot cavities. Nano-bowtie metal-insulator-metal (MIM) substrates [189] demonstrate excellent enhancement of 6× and 24× for parallel and orthogonal coupling, respectively (Figure 10A). This structure contributes to SLR enhancement by confining light in the MIM cavity and forming Fabry-Perot resonances. The nano-bowtie MIM structure is highly sensitive to local changes in refractive index as shown in Figure 10B and C, with sensitivity to a thousandth RIU. In addition, nano-mushroom arrays have been developed for detection of cytochrome C, achieving a LOD of 200 pM (Figure 10D) [190]. Like the nano-bowtie structure, the nano mushroom array is also highly sensitive to changes in the local environment when composition of water-glycerin mixtures are varied as shown in Figure 10E and F. Hybrid structures such as nanowire, nanoring arrays [191] and nanodot arrays [192] in microcavities have a high FOM for biological sensing, while reducing SLR substrate effects.

3.6 Gap plasmon

Surface plasmons that exist and confine high EM energy between two metal structures in a small gap are called gap plasmons (Figure 11). When the metal structures are in close proximity, the near-field coupling dominates and confines the EM field in the nanogap [193, 194]. When the gap increases, the coupling weakens and the properties of the individual metal structures are displayed. Recently, nanostructure arrays coupled with metallics films separated by a spacer layer [195, 196, 15] have gained increasing attention because of their controlled EM over a large tunable wavelength range. The high enhancement of plasmon intensity at the gap is of interest because of its applications in metamaterials, energy transfer, sensors, and solar energy harvesting.

There are two prominent multilayer configurations where gap plasmon can be realized. One is MIM and the other is insulator-metal-insulator (IMI). Both structures

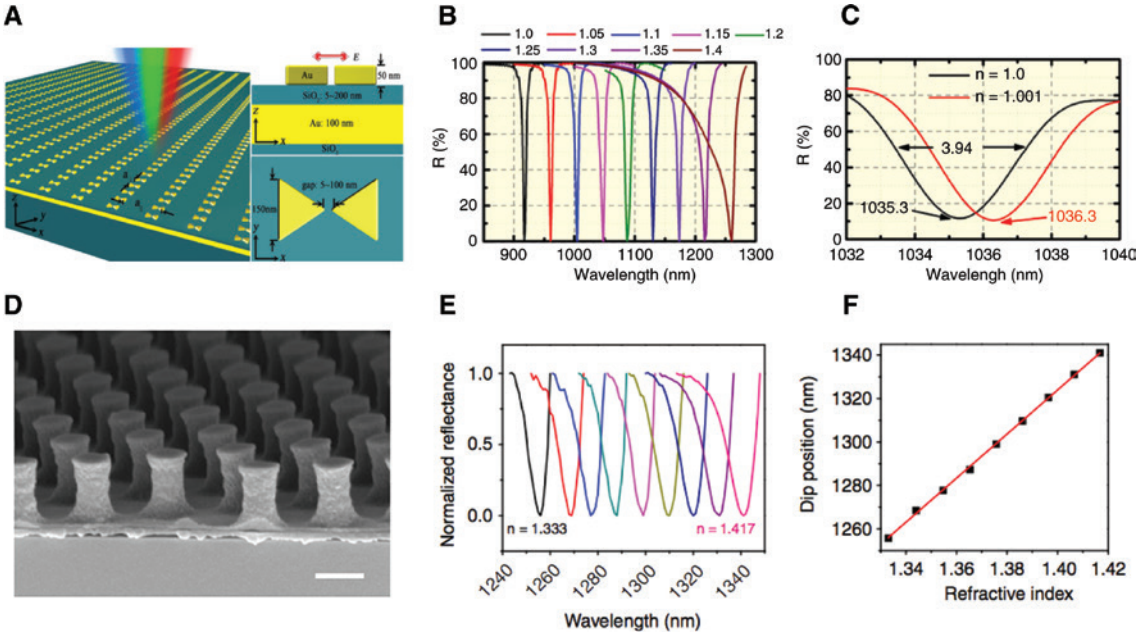

Figure 10: Configuration and optical properties of nano arrays supporting SLR.
(A) Schematic of the Au BNAs with MIM configuration; (B) normalized reflection spectrum of the BNAs as a function of the superstrate refractive index ranging from 1.0 to 1.4; (C) zoom-in reflectance spectra when superstrate refractive index changes from 1.0 to 1.001 (A, B and C reproduced from [189]); (D) SEM image showing cross section of gold nano-mushroom arrays (GMRA); (E) refractive index sensing using the GMRA. Reflectance spectra of the GMRA immersed in glycerin water mixture solutions with varying compositions; (F) relationship between the wavelength of D1 (solid squares) and the refractive index. The line is a linear fit, with the refractive index sensitivity and FOM value determined to be 1015 nm RIU 1 and 80 108, respectively (D, E and F reproduced from [190]).

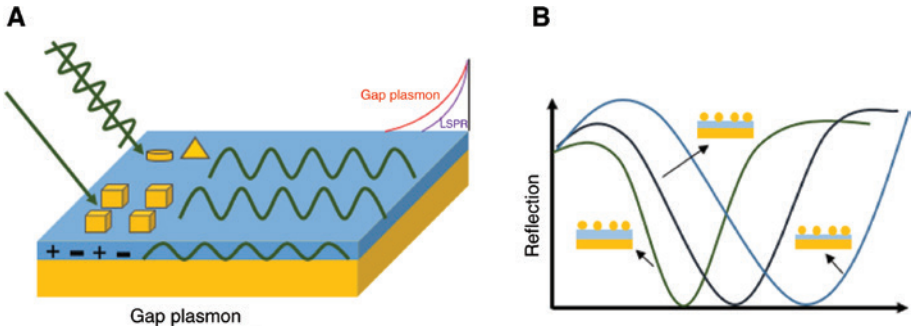

Figure 11: Excitation and optical properties of gap plasmon.
(A) Gap plasmon standing wave exists when two metal structures are closely separated by a spacer layer; (B) gap plasmon leads to large absorption and amplified EM field, depending on the spacer layer thickness.

confine the gap plasmon; however, an MIM configuration is superior in terms of mode volume, strong confinement, and quality factor [197, 198]. In a simple MIM structure, the metal on the illumination side should be thin enough to allow the incident light to enter through the system. Once the light passes through the metal strip, light is trapped in the dielectric layer, forming a standing wave known as a gap plasmon shown in Figure 11A. This shows a strong absorption peak in the spectrum. The gap plasmon can be explained by Fabry-Perot (FP) formula [198, 199]:

$$w\frac{2\pi}{\lambda}n_{\text{eff}} = p\pi + \phi \tag{12}$$

where w is the strip width, p is an integer, λ is the wavelength, n_{eff} is the effective refractive index where gap mode is formed, ϕ is an additional phase shift due to reflection. By tuning the spacer layer thickness, the refractive index absorption peak is tuned over a large wavelength range (Figure 11B). When the space layer is very thin (typically <8 nm), the gap plasmon is very intense due to the strong light confinement. The EM field strength of the gap plasmon decreases with an increase in the thickness of the spacer layer. Thus, there is a range of thickness where an MIM can support a gap plasmon mode.

MIM structures with periodic ordered patterns coupled with a film separated with an insulator are called quasi-3D nanostructure arrays. These materials have much sharper optical peaks and intense EM fields because this pattern creates interactions between SPR modes and gap modes. In conventional LSPR, the EM field decays exponentially with the distance away from the structure. In contrast, the gap mode causes the EM energy to oscillate between magnetic and electric counterparts inside the gap. This feature enables almost same EM field intensity over the entire gap, and the mode volume is the physical size of the gap.

Gap plasmon modes are used in wide variety of applications including total light absorption, solar water splitting, and plexiton generation. Total light absorption and broadband absorption are highly demanded in solar energy harvesting applications. An Ag hole array coupled with an Ag film with a silica space layer acts like a perfect absorber at visible light region for solar energy harvesting (Figure 12A) [200]. The reflection dip can be easily tuned by changing the parameters of the nanohole array and spacer layer thickness (Figure 12B, C). It is well known that the emission efficiency of plasmonic hot electrons is dependent on the local EM field; thus, the strong EM field in the plasmonic gap mode can be used to enhance the hot electron generation [201]. When a hematite film is sandwiched between the Au nanodisc array and the Au film (Figure 12D), a strong plasmon gap mode is generated and is dependent on the thickness of the hematite film (Figure 12E). This structure has been successfully used for solar water splitting [201]. The increase in the IPCE enhancement (Figure 12F) is due to the enhancement of hot electron generation by the plasmonic gap mode. In addition to the applications in energy harvesting, gap plasmons allow designing nonlinear photonic and optoelectronic devices. In an Au film-coupled Au nanopyramid array (Figure 12G), the gap plasmon was tuned by varying the thickness of the nanogap (Figure 12H). Because of its strong EM field over a large area throughout the gap, it can be used to couple SPPs with quantum emitters (QEs) in the strong coupling regime to generating plexitions [15]. Plexitons are coherently coupled plasmons and excitions and produce new optical excitation levels [202]. Figure 12I shows a strong coupling of gap mode with QE (J-aggregate) in the quasi-3D nanostructure array in leading to the formation of a plexiton. This eliminates the high energy loss and weak nonlinearity in the optoelectronic devices.

Plasmonic gap modes are advantageous for SERS sensors due to their high EM enhancement as compared to conventionally used colloidal nanostructures. In a study by Sivashanmugana et al. [203], a hexagonal Au nanorod array fabricated by FIB was coupled with Ag nancubes on the surface, generating gap mode enhancement regions.

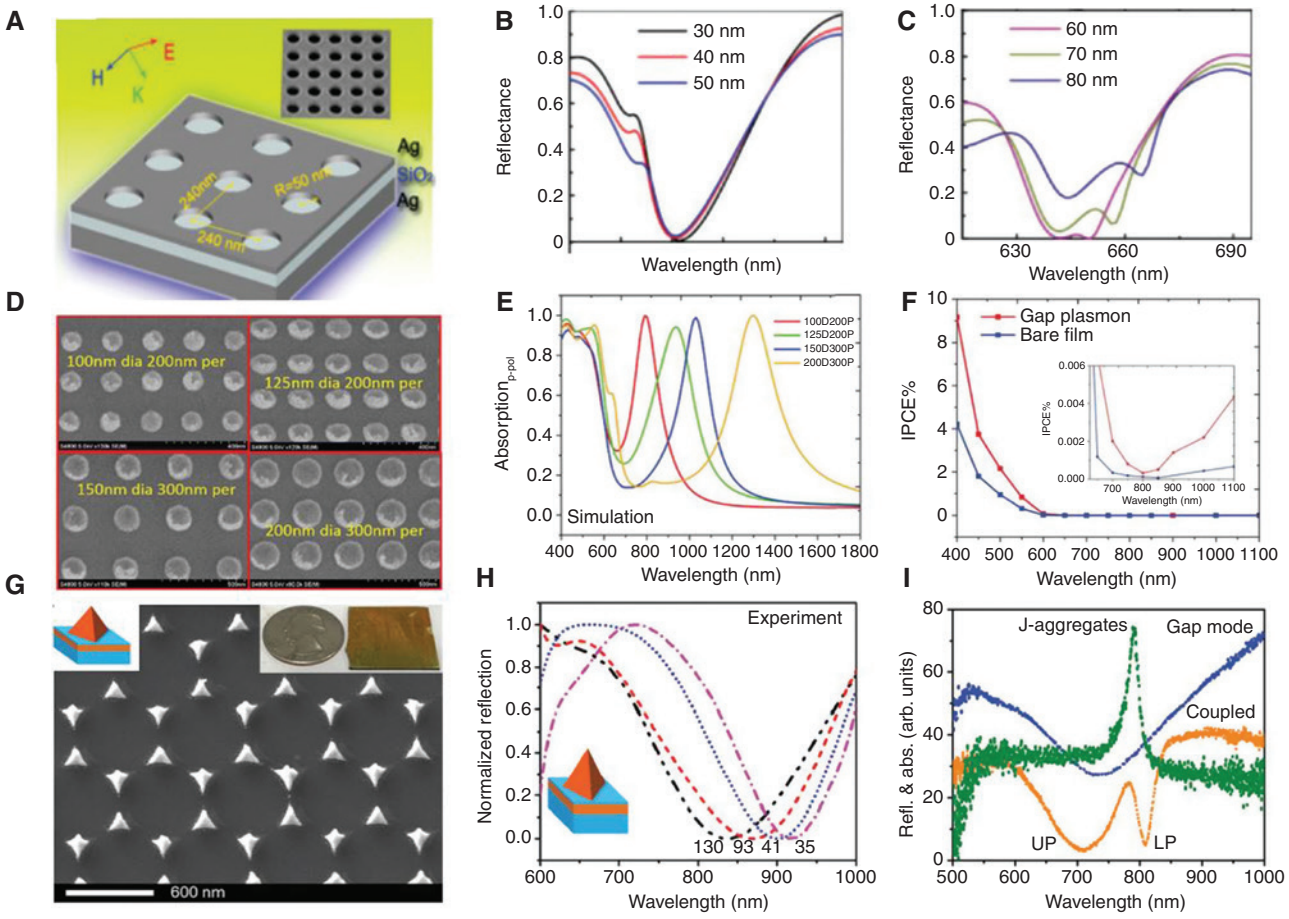

Figure 12: SEM and optical properties of select nano arrays supporting gap plasmon.
(A) Schematic and SEM image (inset) of Ag nanohole array on Ag film with SiO_2 spacer layer; (B, C) experimental reflectance for hole radius changing from 30 to 80 nm. A perfect absorber (99% absorbance) is realized when the hole radius is 50 nm and clear spectral splitting is observed for radius 60 ~ 80 nm (A, B and C reprinted with permission from [200]. Copyright (2012) by the American Physical Society); (D) SEM images of the fabricated Au nanodisks for the gap-plasmon arrays with four different disk diameters (dia: diameter, per: period); (E) experimentally measured absorption spectra of nanodiscs with different disk diameters at 20° incidences for all the arrays; (F) incident photon conversion efficiency (IPCE) comparison between gap plasmon electrode and bare hematite electrode, Inset: IPCE in the near IR wavelengths (D, E and F reproduced from [201] with permission from The Royal Society of Chemistry); (G) SEM image of the fabricated film-coupled Au nanopyramid array (the inset shows the size comparison of quarter coin with sample and schematic nanostructure; (H) experimental reflection spectra of gap plasmon mode with various silica thicknesses the inset shows the side view of schematic nanostructure; (I) experimentally measured spectral profiles of J-aggregates, plasmonic gap modes, and the hybridized upper and lower plexciton states (G, H and I reproduced from [15] with permission from The Royal Society of Chemistry).

A large SERS enhancement of 9.11×10^8 resulted from the plasmonic coupling between the nanogaps of hexagonal edges on the nanorod and nanogap. When applied as an SERS sensor for lung cancer exosomes, an LOD of 10^4–10^5 was achieved, which is lower than that of traditional biochemical analysis. The nanogap modes were optimized by tuning the gap size for maximum EM field enhancement [203]. A 3D SERS substrate [204] inspired by bio-scaffold arrays of cicada wings has been developed with hierarchical nanogaps for viral detection. The Ag nano-islands and Ag nano-flowers with nanogaps on chitin nanopillars have generated high density of hot spots with an enhancement factor of 5.8×10^7. As mentioned, plasmonic gap mode sensors are as not as common. However, fundamental work continues to drive exploration of plasmonic gap modes for sensors. In particular, the LSPR plasmonic gap modes can be tuned into the infrared region with high FOM, showing a potential for SERS application [205].

4 Remarks

The availability of fabrication techniques as well as the discovery and understanding of plasmonic modes are the key to the success of plasmon research. In the past two decades, many fabrication methods have been developed

to overcome the limitation of conventional photolithography. However, significant challenges remain for the massive fabrication of nano-arrays at nanoscale-resolution and low-cost with excellent repeatability, controllability, and great flexibility in tuning optical properties. In many cases, simulation shows that hierarchical structures could exhibit extraordinary optical properties. However, no fabrication method is available to make real nanostructures. In particular, there are still technical barriers for the fabrication of large-area, long-range-ordered periodic nano-array patterns. Additionally, when plasmonic nano-arrays are used in practical application such as photovoltaics, photoelectrochemical cells (PECs), and optoelectronics, plasmonic metal-semiconductor heterojunctions are required to enable plasmonic coupling between metals and semiconductors. Fabrication of the integrated metal-semiconductor heterojunctions often require high-temperature processing, which may destroy the metal nanostructure at high temperature. This puts a constraint on fabrication routes and techniques.

Plasmonic nano-arrays are finding various applications in sensors, photovoltaics, PECs, photodetectors, and other optoelectronics, which require coupling of plasmonic nano-arrays to other components of devices. Unfortunately, plasmonic nano-arrays sometimes are randomly assembled into devices, in which the plasmonic effect has not been utilized effectively. Consequently, this leads to a false image that plasmonics is interesting scientifically but useless in practical applications. To solve this problem, plasmonic applications should be implemented in a manner of "device-by-design". In many cases, the plasmonic effects of nanostructures are not known or understood thoroughly. Theoretical calculation and simulation of EM fields and optical responses are needed to assist the design of plasmonic devices. The "device-by-design" strategy must be built on the prerequisite of full understanding of the concepts and principles of various plasmonic modes and acquaintance of the fabrication techniques of nanostructures.

Rapid progress has been made in 2D and 3D plasmonic nano-arrays in the following aspects [78, 206]: (i) Introduction of new fabrication techniques has made it possible to create new 2D and 3D plasmonic nano-arrays with desirable optical properties; (ii) new plasmonic modes have been discovered; (iii) existing plasmonic modes have gotten better understanding; and (iv) 2D and 3D plasmonic nano-arrays have been finding increasing applications in various fields. One can forecast the continuing growth in these aspects.

In the past two decades, the majority of SPR studies were focused on the nanostructures typically larger than 10 nm. The near-field and far-field plasmonic properties of these relatively large nanostructures are attributed to the classical behaviors of both electrons and EM fields. That is, the dynamics of valence electrons in these nanostructures are considered as a collective harmonic oscillation of the electron charge density; and the corresponding EM fields are described by the framework of Maxwell's equations. Rapid development of fabrication and synthesis techniques has enabled the fabrication and manipulation of particles and other structures down to the molecular and even atomic level. The plasmonic properties of these quantum-sized particles and structures are governed by the complex quantum interactions and dynamics of the electrons other than the classical behaviors of both electrons and EM fields. This has resulted in the emerging of the "quantum plasmonics" field. It is interesting to study the quantum properties of plasmon excited in 2D and 3D periodic array patterns under the quantized condition. Fundamental understanding of the light-matter interactions at the quantum level in these downscale structures will result in new quantum-controlled plasmonic devices.

Acknowledgment: This work was partially supported by the Endowment of George B. Berry Chair of Engineering at West Virginia University, and the National Science Foundation Graduate Research Fellowship under Grant No. DGE-1102689.

Conflict of interest: The authors declare no competing financial interest.

References

[1] Gleiter H. Nanostructured materials: basic concepts and microstructure. Acta Mater 2000;48:1–29.
[2] Maier SA. Plasmonics: fundamentals and applications. New York, NY: Springer, 2007.
[3] Murray WA, Astilean S, Barnes WL. Transition from localized surface plasmon resonance to extended surface plasmon-polariton as metallic nanoparticles merge to form a periodic hole array. Phys Rev B 2004;69:165407, 1–7.
[4] Henglein A. Small particle research: physicochemical properties of extremely small colloidal metal and semiconductor particles. Chem Rev 1989;89:1861–73.
[5] Willets KA, Van Duyne RP. Localized surface plasmon resonance spectroscopy and sensing. Annu Rev Phys Chem 2007;58: 267–97.
[6] Blatchford CG, Campbell JR, Creighton JA. Plasma resonance-enhanced Raman scattering of absorbates on sold colloids: the effects of aggregation. J A Surf Sci 1982;120:435–55.
[7] Xu H, Aizpurua J, Kall M, Apell P. Electromagnetic contributions to single-molecule sensitivity in surface-enhanced Raman scattering. Phys Rev E 2000;62:4318–24.

[8] Kneipp K, Kneipp H, Manoharan R, et al. Extremely large enhancement factors in surface-enhanced Raman scattering for molecules on colloidal gold clusters. Appl Spectrosc 1998;52:1493–7.
[9] Wang W, Ramezani M, Väkeväinen AI, Törmä P, Gómez Rivas J, Odom TW. The rich photonic world of plasmonic nanoparticle arrays. Mater Today 2018;21:303–14.
[10] Zheng P, Cushing SK, Suri S, Wu N. Tailoring plasmonic properties of gold nanohole arrays for surface-enhanced Raman scattering. Phys Chem Chem Phys 2015;17:21211–9.
[11] Van der Zande B, Bohmer MR, Fokkink LGJ, Schonenberger C. Aqueous gold sols of rod-shaped particles. J Phys Chem B 1997;101:852–4.
[12] Zheng P, Kasani S, Wu N. Detection of nitrite with a surface-enhanced Raman scattering sensor based on silver nanopyramid array. Anal Chim Acta 2018;1040:158–65.
[13] Kasani S, Zheng P, Wu N. Tailoring optical properties of large area plasmonic gold nano-ring array pattern. J Phys Chem C 2018;122:13443–9.
[14] Zheng P, Tang H, Liu B, Kasani S, Luang L, Wu N. Origin of strong and narrow localized surface plasmon resonance of copper nanocubes. Nano Res 2019;12:63–8.
[15] Zheng P, Kasani S, Wu N. Converting plasmonic light scattering to confined light absorption and creating plexcitons by coupling a gold nano-pyramid array onto a silica-gold film. Nanoscale Horiz 2019;4:516–25.
[16] Garcia de Abajo F J. Colloquium: Light scattering by particle and hole arrays. Rev Mod Phys 2007;79:1267–90.
[17] Li H, Cullum BM. Dual layer and multilayer enhancements from silver film over nanostructured surface-enhanced Raman substrates. Appl Spectrosc 2005;59:410–7.
[18] Raman CV. A new radiation. Indian J Phys 1928;2:387–98.
[19] Gardiner DJ. Practical Raman spectroscopy. Berlin, Heidelberg: Springer-Verlag, 1989.
[20] Fleischmann M, Hendra PJ, McQuillan AJ. Raman spectra of pyridine absorbed at a silver electrode. Chem Phys Lett 1974;26:163–6.
[21] Kneipp K, Wang Y, Kneipp H, et al. Single molecule detection using surface-enhanced Raman scattering (SERS). Phys Rev Lett 1997;78:1667–70.
[22] Nie S. Probing single molecules and single nanoparticles by surface-enhanced Raman scattering. Emory, Science 1997;275:1102–6.
[23] Chang TH, Nixon P. Record of the 9th Symposium on Electron, Ion and Laser Beam Technology, Berkeley, CA, USA, 1967, 123.
[24] Tseng AA, Chen K, Chen CD, Ma KJ. Electron beam lithography in nanoscale fabrication: recent development. In: IEEE Transactions on Electronics Packaging Manufacturing, Piscataway, NJ, USA, vol. 26, 2003, 141–9.
[25] Atlissimo A. E-beam lithography for micro-/nanofabrication. Biomicrofluidics 2010;4:026503.
[26] Saifullah MSM, Ondarcuhu T, Koltsov DK, Joachim C, Welland ME. A reliable scheme for fabricating sub-5 nm co-planar junctions for single-molecule detection. Nanotechnology 2002;13:659–62.
[27] Broers A, Molzen W, Cuomo J, Wittels N. Electron beam fabrication of 80 Å metal structures. Appl Phys Lett 1976;29:596–8.
[28] Broers A. Fabrication limits of electron beam lithography and of UV, X-ray and ion beam lithographies. Phil Trans R Soc Lond A 1995; 353:291–311.
[29] Arshak K, Mihova M. State-of-the-art focused ion beam nanolithography. J Optoelectron Adv Mat 2005;7:193–8.
[30] Matsui S, Kojima Y, Ochiai Y, Honda T. High-resolution focused ion beam lithography. J Vac Sci Technol B 1991;9:2622–32.
[31] Matsui S, Mori K, Saigo K, Shiokawa T, Toyoda K, Namba S. Lithographic approach for 100 nm fabrication by focused ion beam. J Vac Sci Technol 1986;4:845.
[32] Gamo K. Nanofabrication by FIB. Microelectron Eng 1996;32:159–71.
[33] Piner RD, Zhu J, Xu F, Hong S H, Mirkin CA. "Dip-pen" lithography. Science 1999;283:661–3.
[34] Ginger DS, Zhang H, Mirkin CA. The evolution of dip-pen nanolithography. Angew Chem Int Ed 2004;43:30–45.
[35] Mirkin CA. The power of the pen: development of massively parallel dip-pen nanolithography. ACS Nano 2007;1:79–83.
[36] Salaita K, Wang Y, Fragala J, Vega RA, Liu C, Mirkin CA. Massively parallel dip-pen nanolithography with 55,000-pen two-dimensional arrays. Angew Chem Int Ed 2006;4:7220–3.
[37] Roy S. Fabrication of micro- and nano-structured materials using mask-less processes. J Phys D: Appl Phys 2007;40:413–26.
[38] Rodriquez A, Echeverria M, Ellman M, et al. Laser interference lithography for nanoscale structuring of materials: From laboratory to industry. Microelectron Eng 2009;86:937–40.
[39] Moon JH. Multiple-exposure holographic lithography with phase shift. Appl Phys Lett 2004;85:4184.
[40] Byun I, Kim J. Cost-effective laser interference lithography using a 405 nm AlInGaN semiconductor laser. Micromech Microeng 2010;20:055024.
[41] Helgert M, Burkhardt M, Rudolf K, Steiner R, Brunner R. High-frequent structures generated by interference lithography in the DUV. In: Frontiers in Optics 2004/Laser Science XXII/ Diffractive Optics and Micro-Optics/Optical Fabrication and Testing, OSA Technical Digest. Washington, DC, USA, Optical Society of America, 2004.
[42] O'Reilly TB, Smith HI. Linewidth uniformity in Lloyd's mirror interference lithography systems. J Vac Sci Technol B 2008;26:2131–4.
[43] Pieranki P. Two-dimensional interfacial colloidal crystals. Physical Rev Lett 1980;45:569–72.
[44] Dimitrov AS, Nagayama K. Continuous convective assembling of fine particles into two-dimensional arrays on solid surfaces. Langmuir 1996;12:1303–11.
[45] Rossi RC, Tan MX, Lewis NS. Size-dependent electrical behavior of spatially inhomogeneous barrier height regions on silicon. Appl Phys Lett 2000;77:2698–700.
[46] Hulteen JC, Van Duyne R. Nanosphere lithography: a materials general fabrication process for periodic particle array surfaces. J Vac Sci Technol A 1995;13:1553.
[47] Deckman HW, Dunsmuir JH. Natural lithography. Appl Phys Lett 1982;41:377–9.
[48] Ruan WD, Lu ZC, Ji N, Wang CX, Zhao B, Zhang JH. Facile fabrication of large area polystyrene colloidal crystal monolayer via surfactant-free Langmuir–Blodgett technique. Chem Res Chinese Universities 2007;23:712–4.
[49] Tabatabaei M, Sangar A, Kazemi-Zanjani N, Torchio P, Merlen A, Langugne-Labarthet F. Optical properties of silver and gold tetrahedral nanopyramid arrays prepared by nanosphere lithography. J Phys Chem C 2013;117:14778–86.
[50] Bartlett PN, Birkin PR, Ghanem MA. Electrochemical deposition of microporous platinum, palladium, and cobalt films using polystyrene latex sphere templates. Chem Commun 2000;17:1671–2.

[51] Hulteen JC, Treichel D, Smith M, Duval M, Jenson T, Van-Duyne R. Nanosphere lithography: size-tunable silver nanoparticle and surface cluster arrays. J Phys Chem B 1999;103:3854–63.
[52] Chou SY, Krauss PR, Renstrom P J. Imprint of sub-25 nm via and trenches in polymers. Appl Phys Lett 1995;67:3114.
[53] Chou S, Krauss P. Imprint lithography with sub-10nm feature size and high throughput. Elsevier Sci 1997;35:237–40.
[54] Hua F, Sun Y, Gaur A, et al. Polymer imprint lithography with molecular-scale resolution. Nano Lett 2004;4:2467–71.
[55] Lan H, Ding Y. Nanoimprint lithography. In: Wang M, editor. Lithography. Rijeka: InTech, 2010;457–94.
[56] Colburn M, Johnson S, Stewart M, et al. Step and flash imprint lithography: a new approach to high-resolution patterning. Proc SPIE 1999;3676:379–89.
[57] Malinovskis U, Poplausks R, Apsite I, et al. Ultrathin anodic aluminum oxide membranes for production of dense sub-20 nm nanoparticle arrays. J Phys Chem C 2014;118:8685–90.
[58] Su Z, Zhou W. Formation mechanism of porous anodic aluminium and titanium oxides. Adv Mater 2008;20:3663–7.
[59] Qiu T, Zhang W, Lang X, Zhou Y, Cui T, Chu PK. Controlled assembly of highly Raman-enhancing silver nanocap arrays templated by porous anodic alumina membranes. Small 2009;5:2333–7.
[60] Al-Kaysi RO, Ghaddar TH, Guirad G. Fabrication of one-dimensional organic nanostructures using anodic aluminum oxide templates. J Nanomater 2009, Article ID 436375, 14.
[61] Pimpin A, Srituravanich W. Review on micro- and nanolithography techniques and their applications. Eng J 2011;16:37–56.
[62] Madou MJ. Fundamentals of microfabrication: the science of miniaturization. 2nd ed. New York: CRC Press, 2002.
[63] Gates BD, Xu Q, Stewart M, Ryan D, Willson CG, Whitesides GM. New approaches to nanofabrication: Molding, printing, and other techniques. Chem Rev 2005;105:1171–96.
[64] Altissimo M. E-beam lithography for micro/nanofabrication. Biomicrofluidics 2010;4:3–6.
[65] Liu H, Luo Y, Kong W, et al. Large area deep subwavelength interference lithography with a 35 nm half-period based on bulk plasmon polaritons. Optical Mater Exp 2018;8:199–209.
[66] Whitney AV, Myers BD, Van Duyne RP. Sub-100 nm triangular nanopores fabricated with the reactive ion etching variant of nanosphere lithography and angle-resolved nanosphere lithography. Nano Letters 2004;4:1507–11.
[67] Popat KC, Mor G, Grimes CA, Desai TA. Surface modification of nanoporous alumina surfaces with poly ethylene glycol. Langmuir 2004;20:8035–41.
[68] Powell CJ, Swan JB. Effect of oxidation on the characteristic loss spectra of aluminium and magnesium. Phys Rev 1960;118:640–3.
[69] Pines D, Bohm D. A collective description of electron interactions. I. Magnetic interactions. Physl Rev 1951;82:625–34.
[70] Pines D, Bohm D. A collective description of electron interactions: II. Collective vs individual particle aspects of the interactions. Phys Rev 1952;85:338–53.
[71] Pines D, Bohm D. A collective description of electron interactions: III. Coulomb interactions in a degenerate electron gas. Phys Rev 1953;92:609–26.
[72] Jeanmaire DL, Van Duyne RP. J. Surface Raman spectroelectrochemistry Part 1: Heterocyclic, aromatic, and aliphatic amines absorbed on the anodized silver electrode. Electroanal Chem 1977;8:1–20.
[73] Albrecht MG. Creighton. Anomalously intense Raman spectra of pyridine at a silver electrode. J Am Chem Soc 1977;99:5215–7.
[74] Haes AJ, Van Duyne RP. A Nanoscale optical biosensor: sensitivity and selectivity of an approach based on the localized surface plasmon resonance spectroscopy of triangular silver nanoparticles. J Am Chem Soc 2002;124:10596–604.
[75] Hirsch LR, Jackson JB, Lee A, Halas NJ, West JL. A Whole blood immunoassay using gold nanoshells. Anal Chem 2003;75:2377–81.
[76] Sokolov K, Chumanov G, Cotton TM. Enhancement of molecular fluorescence near the surface of colloidal metal films. Anal Chem 1998;70:3898–905.
[77] Zeng J, Liang D, Cao ZX. Applications of optical fiber SPR sensor for measuring of temperature and concentration of liquids. Proc SPIE 2005;5855:667–70.
[78] Li M, Cushing SK, Wu N. Plasmon-enhanced optical sensors: a review. Analyst 2015;140:386–406.
[79] Anker JN, Hall WP, Lyandres O, Shah NC, Zhao J, Van Duyne RP. Biosensing with plasmonic nanosensors. Nat Mater 2008;7:442–53.
[80] Haes AJ, Van Duyne RP. A unified view of propagating and localized surface plasmon resonance biosensors. Anal Bioanal Chem 2004;379:920–30.
[81] Mie G. Beitrge zur optik tr¨uber medien, speziell kolloidaler metal osungen. Annalen Der Physik 1908;330:377–445.
[82] Gans R. Uber die Form ultramikroskopischer Goldteilchen. Ann Phys 1912;37:881–900.
[83] Camden JP, Dieringer JA, Wang Y, et al. Probing the structure of single-molecule surface-enhanced Raman scattering hot spots. J Am Chem Soc 2008;130:12616–7.
[84] Aravind P, Nitzan A, Metiu H. The interaction between electromagnetic resonances and its role in spectroscopic studies of molecules adsorbed on colloidal particles or metal spheres. Surf Sci 1981;110:189–204.
[85] Jain PK, Huang W, El-Sayed WA. On the universal scaling behavior of the distance decay of plasmon coupling in metal nanoparticle pairs: a plasmon ruler equation. Nano Lett 2007;7:2080–8.
[86] Greeneltch NG, Blaber MG, Henry A, Schatz GC, Van Duyne RP. Immobilized nanorod assemblies: fabrication and understanding of large area surface-enhanced Raman spectroscopy substrates. Anal Chem 2013;85:2297–303.
[87] Hatab NA, Chun-Hway H, Gaddis AL, et al. Free-standing optical gold bowtie nano antenna with variable gap size for enhanced Raman spectroscopy. Nano Lett 2010;10:4952–5.
[88] Jung M, Kim J, Choi Y. Preparation of anodic aluminum oxide masks with size-controlled pores for 2D plasmonic nanodot arrays. J Nanomater 2018;2018:9.
[89] Wang T, Zhang J, Xue P, et al. Nanotransfer printing of gold disk, ring and crescent arrays and their IR range optical properties. J Mater Chem C 2014;2:2333–40.
[90] Xie W, Qiu P, Mao C. Bio-imaging, detection and analysis by using nanostructures as SERS substrates. J Mater Chem 2011;21:5190–202.
[91] Kahraman M, Mullen ER, Korkmaz A, Wachsmann-Hogiu S. Fundamentals and applications of SERS-based bioanalytical sensing. Nanophotonics 2017;6:831–52.
[92] Jeon TY, Kim DJ, Park SG, Ki SH, Kim DH. Nanostructured plasmonic substrates for use as SERS sensors. Nano Convergence 2016:3:18.

[93] Sharma B, Frotiera R, Henry A, Ringe R, Van Duyne RP. SERS: Materials applications and the future. Mater Today 2012;5:1–2.
[94] Marks H, Schechinger M, Garza J, Locke A, Cote G. Surface enhanced Raman spectroscopy (SERS) for in vitro diagnostic testing at the point of care. Nanophotonics 2017;6:681–701.
[95] Li M, Cushing SK, Liang H, Suri S, Ma D, Wu N. Plasmonic nanorice antenna on triangle nano-array for surface-enhanced Raman scattering detection of hepatitis B virus DNA. Anal Chem 2013;85:2072–8.
[96] Zheng P, Kasani S. Shi X, et al. Detection of nitrite with a surface-enhanced Raman scattering sensor based on silver nanopyramid array. Anal Chim Acta 2018;1040:158–65.
[97] Li M, Cushing SK, Zhang J, et al. Three-dimensional hierarchical plasmonic nano-architecture enhanced surface-enhanced Raman scattering immunosensor for cancer biomarker detection in blood plasma. ACS Nano 2013;7:4967–76.
[98] Zhang X, Dai Z, Si S, et al. Ultrasensitive SERS substrate integrated with uniform subnanometer scale “hot spots” created by a graphene spacer for the detection of mercury ions. Small 2017;13:1603347.
[99] Zhao Y, Zhao S, Zhang L, Liu Y, Li X, Lu Y. A three-dimensional Au nanoparticle-monolayer graphene-Ag hexagon nano-array structure for high-performance surface-enhanced Raman scattering. RSC Adv 2017;7:11904–12.
[100] Gao X, Zheng P, Kasani S, et al. Paper-based surface-enhanced Raman scattering lateral flow strip for detection of neuron-specific enolase in blood plasma. Anal Chem 2017;89:10104–10.
[101] Li M, Cushing S K, Zhang J, et al. Shape-dependent surface-enhanced Raman scattering in gold-Raman-probe-silica sandwiched nanoparticles for biocompatible applications. Nanotechnology 2012;23:115501–11.
[102] Park JE, Lee Y, Nam JM. Precisely shaped, uniformly formed gold nanocubes with ultrahigh reproducibility in single-particle scattering and surface-enhanced Raman scattering. Nano Lett 2018;18:6475–82.
[103] Scarabelli L, Coronado-Puchau M, Giner-Casares JJ, Langer J, Liz-Marzá LM. Monodisperse gold nanotriangles: size control, large-scale self-assembly, and performance in surface-enhanced Raman scattering. ACS Nano 2014;8:5833–42.
[104] Chen S, Liu D, Wang Z, Sun X, Cui D, Chen X. Picomolar detection of mercuric ions by means of gold silver core shell nanorods. Nanoscale 2013;5:6731–5.
[105] Barnes WL, Dereux A, Ebbesen TW. Surface plasmon subwavelength optics. Nature 2003;424:824–30.
[106] Agranovich VM, Mills DL. Surface polaritons: electromagnetic waves at surfaces and interfaces. North-Holland, Amsterdam, 1982.
[107] Boardman AD. Electromagnetic surface modes. Hoboken, NJ, USA, John Wiley & Sons, 1982.
[108] Raether H. Surface plasmons. Springer Tracts in Modern Physics 1988;111:1. Springer.
[109] Otto A. Spectra of plasmon polaritons at metal-insulator interfaces of a nanosized gold film: expansion into components and their systematization. Z Phys 1968;216:398–410.
[110] Kretschmann E, Raether H. Radiative decay of nonradiative surface plasmons excited by light z. Nature A 1968;23: 2135–6.
[111] Lackowicz JR. Plasmonics in biology and plasmon-controlled fluorescence. Plasmonics 2006;1:5–33.
[112] Dostalek J, Knoll W. Biosensors based on surface plasmon-enhanced fluorescence spectroscopy. Biointerphases 2008;3:12–22.
[113] Zhang J, Zhang L, Xu W. Surface plasmon polaritons: physics and applications. J Phys D: Appl Phys 2012;45:113001.
[114] Ebbesen TW, Lezec H, Ghaemi HF, Thio T, Wolff PA. Extraordinary optical transmission through sub-wavelength hole arrays. Nature 1998;391:667–9.
[115] Fang Y, Sun M. Nanoplasmonic waveguides: towards applications in integrated nanophotonic circuits. Light Sci Appl 2005;4:294.
[116] Zheng P, Cushing SK, Suri S, Wu N. Tailoring plasmonic properties of gold nanohole arrays for surface-enhanced Raman scattering. Phys Chem Chem Phys 2015;17:21211–9.
[117] Kalachyova Y, Mares D, Lyutakov O, Kostejn M, Lapcak L, Svorcik V. Surface plasmon polaritons on silver gratings for optimal SERS response. J Phys Chem C 2015;119:9506–12.
[118] Haynes CL, McFarland AD, van Duyne RP. Surface-enhanced: Raman spectroscopy. Analytical Chem 2005;77:338–46.
[119] Zijlstra P, Chon JWM, Gu M. Five-dimensional optical recording mediated by surface plasmons in gold nanorods. Nature 2009;459:410–3.
[120] Grubisha DS, Lipert R, Park HY, Driskill J, Porter M. Femtomolar detection of prostate-specific antigen: an immunoassay based on surface-enhanced Raman scattering and immunogold labels. Anal Chem 2003;75:5936–43.
[121] Yun L, Qiang L, Shimeng C, Fang C, Hanqi W, Wei P. Surface plasmon resonance biosensor based on smart phone platforms. Sci Rep 2015;5:12864.
[122] Valsecchi C, Armas LEG, Menezes JW. Large area nanohole arrays for sensing fabricated by interference lithography. Sensors 2019;19:2182.
[123] Brolo AG, Gordon R, Leathem B, Kavanagh KL. Surface plasmon sensor based on the enhanced light transmission through arrays of nanoholes in gold films. Langmuir 2004;20:4813–5.
[124] Liang Y, Zhang S, Cao Y, Lu Y, Xu T. Free-standing plasmonic metal-dielectric-metal bandpass filter with high transmission efficiency. Sci Rep 2017;7:4357.
[125] Frederich H, Wen F, Laverdant J, et al. Determination of the surface plasmon polariton extraction efficiency from a self-assembled plasmonic crystal. Plasmonics 2014;9:917.
[126] Dhawan A, Canva M, Vo-Dinh T. Narrow groove plasmonic nano-gratings for surface plasmon resonance sensing. Opt Exp 2011;19:787–1.
[127] Lin L. Manipulation of near field propagation and far field radiation of surface plasmon polariton. Singapore: Springer, 2017.
[128] Xiao C, Chen Z, Qin M, Zhang D, Fan L. Composite sinusoidal nanograting with long-range SERS effect for label-free TNT detection. Photonic Sensors 2018;8:278–88.
[129] Chu Y, Banaee MG, Crozier KB. Double-resonance plasmon substrates for surface-enhanced Raman scattering with enhancement at excitation and stokes frequencies. ACS Nano 2010;4:2804–10.
[130] Du L, Zhang X, Mei T, Yuan X. Localized surface plasmons, surface plasmon polaritons, and their coupling in 2D metallic array for SERS. Optics Exp 2010;18:1959–65.
[131] Wang J, Lin W, Cao E, Xu X, Liang W, Zhan X. Surface plasmon resonance sensors on Raman and fluorescence spectroscopy. Sensors 2017;17:2719.
[132] Miroschnichenko A, Flach S, Kivshar YS. Fano resonances in nanoscale structures. Rev Mod Phys 2010;82:2257–98.

[133] Fano U. Effects of configuration interaction on intensities and phase shifts. Phys Rev 1961;124:1866–78.
[134] Fano U. On the absorption spectrum of noble gases at the edge of the arc spectrum. Nuovo Cimento 1935;12:154–61.
[135] Giannini V, Fernández-Domínguez AI, Sonnefraud Y, Roschuk T, Fernández-García R, Maier SA. Controlling light localization and light-matter interactions with nanoplasmonics. Small 2010;6:2498–507.
[136] Limonov MF, Rybin MV, Poddubny AN, Kivshar YS. Fano resonances in photonics. Nature Photonics 2017;11:543–54.
[137] Luk'yanchuk B, Zheludev NI, Maier SA, et al. The Fano resonance in plasmonic nanostructures and metamaterials. Nature Mater 2010;9:707–15.
[138] Fan JA, Wu C, Bao K, et al. Self-assembled plasmonic nanoparticle clusters. R Science 2010;328:1135–8.
[139] Neubrech F, Pucci A, Cornelius TW, Karim S, García-Etxarri A, Aizpurua J. Resonant plasmonic and vibrational coupling in a tailored nanoantenna for infrared detection. J Phys Rev Lett. 2008;101:157403–7.
[140] Shapiro M. Electromagnetically induced transparency with structured multicontinua. Phys Rev A 2007;75:013424–33.
[141] Neubrech F, Weber D, Enders D, Nagao T, Pucci A. Antenna sensing of surface phonon polaritons. J Phys Chem C 2010;114:7299–301.
[142] Gallinet B, Lovera A, Siegfried T, Sigg H, Martin OJF. Fano resonant plasmonic systems: Functioning principles and applications. AIP Conf Proc 2012;1475:18–20.
[143] Fano U. The theory of anomalous diffraction grating and of quasi-stationary waves on metallic surfaces (Sommerfeld's waves). J Opt Soc Am 1941;31:213–22.
[144] Ho CC, Zhao K, Lee TY. Quasi-3D gold nanoring cavity arrays with high-density hot-spots for SERS applications via nanosphere lithography. Nanoscale 2014;6:8606–11.
[145] Zhao W, Jiang H, Liu B, Jiang Y, Tang C, Li J. Fano resonance based optical modulator reaching 85% modulation depth. Appl Phys Lett 2015;107:171109.
[146] Cui A, Liu Z, Li J, et al. Directly patterned substrate-free plasmonic "nanograter" structures with unusual Fano resonances. Light: Sci Appl 2015;4:308.
[147] Hentschel M, Saliba M, Vogelgesang R, Giessen H, Alivisatos AP, Liu N. Transition from isolated to collective modes in plasmonic oligomers. Nano Lett 2010;10:2721–6.
[148] Zhao W, Ju D, Jiang Y, Zhan Q. Dipole and quadrupole trapped modes within bi-periodic silicon particle array realizing three-channel refractive sensing. Opt Exp 2014;22:31277–85.
[149] Zhan S, Peng Y, He Z, et al. Tunable nanoplasmonic sensor based on the asymmetric degree of Fano resonance in MDM waveguide. Sci Rep 2016;6:22428.
[150] Huang T, Zeng S, Zhao X, Cheng Z, Shum PP. Fano resonance enhanced surface plasmon resonance sensors operating in near-infrared. Photonics 2018;5:23.
[151] Chen J, Gan F, Wang Y, Li G. Plasmonic sensing and modulation based on Fano resonances. Adv Opt Mater 2018;6:1701152.
[152] Zhang S, Bao K, Halas N, Xu H, Nordlnader P. Substrate induced Fano resonances of a plasmonic nanosub: a route to increased sensitivity localized surface plasmon resonance sensors revealed. Nano Lett 2011;11:1657–63.
[153] Cetin AE, Altug H. Fano resonant ring/disk plasmonic nanocavities on conducting substrates for advanced biosensing. ACS Nano 2012;6:9989–95.
[154] Deng H, Chen X, Xu Y, Miroshnichenko AE. Single protein sensing with asymmetric plasmonic hexamer via Fano resonance enhanced two-photon luminescence. Nanoscale 2015;7:20405–13.
[155] Yanik AA, Cetin AE, Huang M. Seeing protein monolayers with naked eye through plasmonic Fano resonances. Proc Natl Acad Sci USA 2011;108:11784–9.
[156] Matsko AB, Savchenkov AA, Strekalov D, Ilchenko VS, Maleki L. Review of applications of whispering-gallery mode resonators in photonics and nonlinear optics. IPN Prog Rep 2005;42:1–51.
[157] Matsko AB, Ilchenko VS. Optical resonators with whispering gallery modes I: basics. IEEE J Sel Top Quantum Electron 2006;12:3.
[158] Ilchenko VS, Matsko AB. Optical resonators with whispering-gallery modes-part II: applications. IEEE J Sel Top Quantum Electron 2006;12:15–32.
[159] Chiasera A, Dumeige Y, Féron P, et al. Spherical whispering-gallery-mode microresonators. Laser Photonics Rev 2010;4:457–82.
[160] Féron P. Whispering gallery mode lasers in erbium doped fluoride glasses. Ann Fond Louis Brogl 2004;29:317–29.
[161] Foreman MR, Swaim JD, Vollmer F. Whispering gallery mode sensors. Adv Opt Photonics 2015;7:168–240.
[162] Arnold S, Khoshsima M, Teraoka I. Shift of whispering-gallery modes in microspheres by protein adsorption. Opt Lett 2003;28:272–4.
[163] Vollmer F, Arnold S. Whispering-gallery mode biosensing: label free detection down to the single molecules. Nat Meth 2008;5:591–6.
[164] Vollmer F, Arnold S, Keng D. Single virus detection from the reactive shift of a whispering-gallery mode. Proc Natl Acad Sci USA 2008;105:20701–4.
[165] Ausman LK, Schatz GC. Whispering-gallery mode resonators: Surface enhanced Raman scattering without plasmons. J Chem Phys 2008;129:054704.
[166] Fan H, Xia C, Fan L, Wang L, Shen M. Graphene supported plasmonic whispering-gallery mode in a metal-coated microcavity for sensing application with ultrahigh sensitivity. Opt Commun 2018;410:668–73.
[167] Kang TY, Lee W, Ahn H, et al. Plasmon coupled whispering gallery modes on nanodisk arrays for signal enhancements. Sci Rep 2017;7:11737.
[168] Schweinsberg A, Hodce S, Lepeshkin N, Boyd R, Chase C, Fajardo J. An environmental sensor based on an integrated optical whispering gallery mode risk resonator. Sens Actuators 2007;123:727–32.
[169] Li C, Teimourpoura MH, McLeod E, Sua J. Enhanced whispering gallery mode sensors. Proc SPIE 2018;10629:201.
[170] Min B, Ostby E, Sorger V. High-Q surface-plasmon-polariton whispering-gallery microcavity. Nature 2009;457:455–8.
[171] Arnold S, Dantham VR, Barbre C, Garetz BA, Fan X. Periodic plasmonic enhancing epitopes on a whispering gallery mode biosensor. Opt Exp 2012;20:26147–59.
[172] Vesseur EJR, Garcia de Abajo FJ, Polman A. Modal decomposition of surface-plasmon whispering gallery resonators. Nano Lett 2009;9:3147–50.
[173] Dantham VR, Holler S, Barbre C, Keng D, Kolchenko V, Arnold S. Label-free detection of single protein using a nanoplasmonic photonic hybrid microcavity. Nano Lett 2013;13:3347–51.

[174] Bozzola A, Perotto S, De Angelis F. Hybrid plasmonic-photonic whispering gallery mode resonators for sensing: a critical review. Analyst 2017;142:883–98.
[175] Vahala KJ. Optical microcavities. Nature 2003;424:839–46.
[176] Noda S, Fujita M, Asano T. Spontaneous-emission control by photonic crystals and nanocavities. Nature Photon 2007;1:449–58.
[177] Lin LH, Zheng YB. Engineering of parallel plasmonic-photonic interactions for on-chip refractive index sensors. Nanoscale 2015;7:12205–14.
[178] Kravets VG, Kabashin AV, Barnes WL, Grigorenko AN. Plasmonic surface lattice resonances: a review of properties and applications. Chem Rev 2018;118:5912–51.
[179] Rajeeva BB, Lin L, Zheng Y. Design and applications of lattice plasmon resonances. Nano Res 2018;11:4423–40.
[180] Humphrey AD, Barnes WL. Plasmonic surface lattice resonances on arrays of different lattice symmetry. Phys Rev B: Condens Matter Mater Phys 2014;90:075404–12.
[181] Haynes CL, McFarland AD, Zhao LL, et al. Nanoparticle optics: The importance of radiative dipole coupling in two-dimensional nanoparticle arrays. J Phys Chem B 2003;107:7337–42.
[182] Humphrey A, Meinzer N, Starkey RA, Barnes WL. Surface lattice resonances in plasmonic arrays of asymmetric disc dimers. ACS Photonics 2016;3:634–9.
[183] Zhukovsky SV, Babicheva VE, Uskov AV, Protsenko IE, Lavrinenko AV. Enhanced electron photoemission by collective lattice resonances in plasmonic nanoparticle-array photodetectors and solar cells. Plasmonics 2014;9:283–9.
[184] Lin L, Zheng Y. Optimizing plasmonic nanoantennas via coordinated multiple coupling. Sci Rep 2015;5:14788.
[185] Ng C, Dligatch S, Amekura H, Davis TJ, Gośmez DE. Waveguide-plasmon polariton enhanced photochemistry. Adv Opt Mater 2015;3:1582–90.
[186] Sadeghi SM, Wing WJ, Campbell Q. Tunable plasmonic-lattice mode sensors with ultrahigh sensitivities and figures of merits. J Appl Phys 2016;119:244503–5.
[187] Gutha R, Sadeghi S, Sharp C, Wing WJ. Biological sensing using hybridization phase of plasmonic resonances with photonic lattice modes in arrays of gold nanoantennas. Nanotechnology 2017;28:355504–11.
[188] Kuznetsov AI, Evlyukhin AB, Goncalves MR, et al. Laser fabrication of large-scale nanoparticle arrays for sensing applications. ACS Nano 2011;5:4843–9.
[189] Lin LH, Zheng YB. Optimizing plasmonic nanoantennas via coordinated multiple coupling. Sci Rep 2015;5:14788.
[190] Shen Y, Zhou JH, Liu TR, et al. Plasmonic gold mushroom arrays with refractive index sensing figures of merit approaching the theoretical limit. Nat Commun 2013;4:2381.
[191] Li ZY, Butun S, Aydin K. Ultranarrow band absorbers based on surface lattice resonances in nanostructured metal surfaces. ACS Nano 2014;8:8242–8.
[192] Bahramipanah M, Dutta-Gupta S, Abasahl B, Martin OJF. Cavity-coupled plasmonic device with enhanced sensitivity and figure-of-merit. ACS Nano 2015;9:7621–33.
[193] Søndergaard T, Jung J, Bozhevolnyi SI, Della Valle G. Theoretical analysis of gold nano-strip gap plasmon resonators. N J Phys 2008;10:105008.
[194] Li GC, Zhang YL, Lei DY. Hybrid plasmonic gap modes in metal film-coupled dimers and their physical origins revealed by polarization resolved dark field spectroscopy. Nanoscale 2016;8:7119–26.
[195] Cesario J, Quidant R, Badenes G, Enoch S. Electromagnetic coupling between a metal nanoparticle grating and a metallic surface. Opt Lett 2005;30:3404–6.
[196] Norlander P, Le F. Plasmonic structure and electromagnetic field enhancements in the metallic nanoparticle-film system. Appl Phys B 2006;84:35–41.
[197] Bozhevolnyi SI. Effective-index modeling of channel plasmon polaritons. Opt Exp 2006;14:9467–76.
[198] Søndergaard T, Bozhevolnyi S. Slow-plasmon resonant nanostructures scattering and field enhancements. Phys Rev B 2007;75:073402–8.
[199] Chang SW, Lin TR, Chuang SL. Theory of plasmonic Fabry-Perot nanolasers. Opt Exp 2010;18:15039–53.
[200] Fang Z, Zhen YR, Fan L, Zhu X, Nordlander P. Tunable wide-angle plasmonic perfect absorber at visible frequencies. Phys Rev B 2012;85:245401.
[201] Dutta A, Naldoni A, Malara F, Govorov AO, Shalaev V, Boltasseva A. Gap-plasmon enhanced water splitting with ultrathin hematite films: the role of plasmonic-based light trapping and hot electrons. Faraday Discuss 2019;214:283–95.
[202] Fofang NT, Grady NK, Fan Z, Govorov AO, Halas NJ. Plexciton Dynamics: exciton plasmon coupling in a J-aggregate Au nanoshell complex provides a mechanism for nonlinearity. Nano Lett 2011;11:1556–60.
[203] Sivashanmugana K, Huang WL, Lina CH, et al. Bimetallic nanoplasmonic gap-mode SERS substrate for lung normal and cancer-derived exosomes detection. J Taiwan Inst Chem Eng 2017;80:149–55.
[204] Kubo W, Fujikawa S. Au double nanopillars with nanogap for plasmonic sensor. Nano Lett 2011;11:8–15.
[205] Shao F, Lu Z, Liu C, et al. Hierarchical nanogaps within bioscaffold arrays as a high- performance SERS substrate for animal virus biosensing. ACS Appl Mater Interfaces 2014;6:6281–9.
[206] Wu N. Plasmonic metal-semiconductor photocatalysts and photoelectrochemical cells: a review. Nanoscale 2018;10:2679–96.